

USE FILE COPY

①

1990

Thesis/Dissertation

A Case Study of the 19 October 1989 Polar Cap Absorption
Event Using the Imaging Riometer for Ionospheric Studies

Timothy C. Davis

AFIT Student at: University of Maryland

AFIT/CI/CIA - 90-076

AD-A227 764

AFIT/CI
Wright-Patterson AFB OH 45433

Approved for Public Release IAW AFR 190-1
Distribution Unlimited
ERNEST A. HAYGOOD, 1st Lt, USAF
Executive Officer, Civilian Institution Programs

DTIC
ELECTE
OCT 23 1990
S B D
CT

ABSTRACT

Title of Thesis: A CASE STUDY OF THE 19 OCTOBER 1989 POLAR CAP
ABSORPTION EVENT USING THE IMAGING RIOMETER
FOR IONOSPHERIC STUDIES (103 pages)

Name of degree candidate: Timothy C. Davis, Captain, USAF

Degree and Year: Master of Science, 1990

Institution: University of Maryland, College Park

Thesis directed by: Professor Theodore J. Rosenberg, Research Professor

Institute for Physical Science and Technology

University of Maryland

A polar cap absorption (PCA) event, beginning on 19 October 1989, is examined using the Imaging Riometer for Ionospheric Studies (IRIS) developed at the University of Maryland. IRIS is a 49-beam (7×7) phased-array 38.2 MHz radiowave imaging system and operating at Amundsen-Scott South Pole Station, Antarctica. After applying a low-pass (>10 minute) filter, we perform a cross-correlation between the central beam and the other beams in the array. From the cross-correlation analysis, we attempt to determine whether there is any delay of effects during event onset and early main phase (plateau) within the array. For most of the period studied, no delay was detected; *i.e.* features of each beam's absorption time series were essentially simultaneous. However, significant delays (~ 2 minutes) occurred at the equatorward edge during a local absorption peak

occurring just prior to magnetic local noon. The peak is coincident with short-term energetic particle flux enhancements detected by GOES-7. Two possible mechanisms are proposed: a local time variation of cutoff rigidities possibly associated with the relative position of the dayside cusp, and a short-term change in energetic particle rigidity spectrum. The result begs further investigation of this and subsequent events using these and other data sources.



Accession For	
NTIS GRA&I	<input checked="" type="checkbox"/>
DTIC TAB	<input type="checkbox"/>
Unannounced	<input type="checkbox"/>
Justification _____	
By _____	
Distribution/	
Availability Codes	
Dist	Avail and/or Special
A-1	

A CASE STUDY OF THE 19 OCTOBER 1989
POLAR CAP ABSORPTION EVENT USING
THE IMAGING RIOMETER FOR
IONOSPHERIC STUDIES

by

Timothy C. Davis

Thesis submitted to the Faculty of the Graduate School
of the University of Maryland in partial fulfillment
of the requirements for the degree of
Master of Science
1990

Advisory Committee:

Professor Theodore J. Rosenberg, Chairman/Advisor
Professor Anandu D. Vernekar
Associate Professor Robert G. Ellingson

ABSTRACT

Title of Thesis: A CASE STUDY OF THE 19 OCTOBER 1989 POLAR CAP
ABSORPTION EVENT USING THE IMAGING RIOMETER
FOR IONOSPHERIC STUDIES

Timothy C. Davis, Master of Science, 1990

Thesis directed by: Professor Theodore J. Rosenberg

Institute for Physical Science and Technology

A polar cap absorption (PCA) event, beginning on 19 October 1989, is examined using the Imaging Riometer for Ionospheric Studies (IRIS) developed at the University of Maryland. IRIS is a 49-beam (7×7) phased-array 38.2 MHz radiowave imaging system and operating at Amundsen-Scott South Pole Station, Antarctica. After applying a low-pass (>10 minute) filter, we perform a cross-correlation between the central beam and the other beams in the array. From the cross-correlation analysis, we attempt to determine whether there is any delay of effects during event onset and early main phase (plateau) within the array. For most of the period studied, no delay was detected; *i.e.* features of each beam's absorption time series were essentially simultaneous. However, significant delays

(~2 minutes) occurred at the equatorward edge during a local absorption peak occurring just prior to magnetic local noon. The peak is coincident with short-term energetic particle flux enhancements detected by GOES-7. Two possible mechanisms are proposed: a local time variation of cutoff rigidities possibly associated with the relative position of the dayside cusp, and a short-term change in energetic particle rigidity spectrum. The result begs further investigation of this and subsequent events using these and other data sources.

Acknowledgements

I wish to express my deepest gratitude to the many people who helped during this effort and during my time at College Park. First and foremost, thanks to Sharon, my wife, for her love, encouragement, and faith, even at times when I probably deserved none of it. I am indebted to my two sons, Shawn and Nathan, for bringing me back down to earth from the ionosphere upon entering the front door every evening. Finally, thanks to my parents for demanding that I stop worrying and for being there when I've needed encouragement over the past 30 years. All these people make me realize what really is important in life.

Special thanks go to Dr. Ted Rosenberg, Dan Detrick, and Dr. Qian Wu of the Institute for Physical Science and Technology. Without their help, guidance, and knowhow, this study would never have gotten anywhere. Additionally, my heart goes out to all the scientists and technicians at South Pole Station for their sacrifices and dedication to help us better understand our planet.

To my friends and officemates, thanks for the comraderie and moral support. Last, but definitely not least, I wish to thank the United States Air Force and the American taxpayers for giving me the opportunity for further study.

Design and installation of the IRIS project were supported by NSF grants DPP 8419272 and DPP 8818229, respectively.

Contents

1	Introduction	1
2	Solar Protons and Their Earthbound Journey	4
2.1	The Sun and Solar Flares	4
2.2	Travel of Plasma Through the Interplanetary Medium	7
2.2.1	The Interplanetary Magnetic Field (IMF) and The Solar Wind	9
2.2.2	The Neutral Sheet	12
2.3	Interaction with the Magnetosphere	15
2.3.1	Structure of the Magnetosphere	15
2.3.2	Entry of Solar Energetic Particles into the Magnetosphere	17
2.3.3	Trapped Radiation	22
2.3.4	Geomagnetic Storms and Aurora	23
3	The Ionosphere	28
3.1	Ionospheric Layers and Chapman Theory	30
3.1.1	The E-Region	30

3.1.2	The F-Region	32
3.1.3	The D-Region	32
3.2	Ionospheric Radiowave Propagation	33
3.2.1	Ionospheric Refraction of Radio Waves	33
3.2.2	Absorption	34
3.3	Enhanced D-Region Ionization	39
3.3.1	The Sudden Ionospheric Disturbance	43
3.3.2	Auroral Zone Absorption	43
3.4	Solar Proton Events and Polar Cap Absorption	44
3.4.1	Brief History	44
3.4.2	Ionospheric Effects	51
4	Instrumentation and Data Sources	56
4.1	Satellite-Borne Sensors	56
4.2	Ground-Based Sensors	57
4.2.1	Magnetometer	58
4.2.2	Riometers	58
4.2.3	The University of Maryland Imaging Riometer for Ionospheric Studies (IRIS)	63
5	Examination of a PCA Event Using IRIS	68
5.1	The Game Plan	68
5.1.1	Filtering the Data	69
5.1.2	Beam Cross-Correlation	70

5.1.3	Visual Inspection of the Imaged Data	72
5.1.4	Limitations and Assumptions	72
5.2	The Solar Flare of 19 October 1989	74
5.2.1	Near-Earth Particle Environment	74
5.2.2	Examination of Magnetometer Data	76
5.2.3	Examination of the IRIS Data	76
5.2.4	Results of the Cross-Correlation Analysis	79
5.2.5	Discussion of the Imaged Data	89
5.3	Discussion	92
5.4	Suggestions for Future Research	95

List of Figures

2.1	A solar flare model, showing possible sources for some known flare products (from Hargreaves, 1979, after Piddington, 1969).	6
2.2	Diagram of solar flare products and near-earth effects (from Mitra, 1974).	8
2.3	Archimedean spiral structure of the IMF in (a) stationary reference plane and (b) rotating with the sun, showing plasma flow and magnetic field structure (from Hundhausen, 1972).	11
2.4	Formation of a neutral sheet. Earth is pictured above (north of) the sheet (from Townsend <i>et al.</i> , 1982).	13
2.5	Warped neutral sheet; solid (dashed) lines lie above (below) ecliptic plane (from Bruzek and Durrant, 1977).	14
2.6	A magnetospheric model (from Bruzek and Durrant, 1977).	16

2.7	Three dimensional view of magnetosheath plasma inside the magnetopause. This diagram depicts an IMF with southward component and shows how the IMF and geomagnetic fields connect on the dayside via X-type reconnection. Notice how field lines map down into the auroral and polar regions (from Heikkila, 1985). . .	18
2.8	The polar cleft, distinct from the cusp in that it has greater extent in local time, whereas the cusp is relatively small and isolated near local noon (from Heikkila, 1985).	19
2.9	Dungey reconnection model for southward and northward IMF. X-type neutral points are labelled <i>N</i> , and arrows denote motion of field lines during the reconnection process (from Russell, 1987).	21
2.10	Inner and outer radiation belt zones from Pioneer IV. Contours are geiger counting rates. The inner zone consists of high energy (some with $E > 30$ MeV) protons; the outer zone consists of solar wind particles, some in excess of 1.5 MeV (from Hargreaves, 1979, after Van Allen and Frank, 1959).	24
2.11	Average auroral oval position for various times of the day. The small cross is the south geomagnetic pole; the circled cross is South Pole Station (geographic pole). The solar direction is toward the top of the figure (from Rairden and Mende, 1989).	27

3.1	Typical midlatitude ionospheric electron density profiles during solar maximum and minimum, day and night. Different altitude regions are labeled D , E , F_1 , and F_2 (from Richmond, 1987).	29
3.2	Chapman layer formation process, where q is ion production rate, I_λ is the specific intensity of ionizing radiation, and ρ_m is neutral particle density.	31
3.3	Application of Snell's Law to a stratified medium where electron density is increasing with height.	35
3.4	A wave approaching a layer of charged particles from below. The concentration of charged particles increases upward. Since μ decreases upward and $V_p = c/\mu$, the top of the wave (A) travels more rapidly than the bottom (B) so the wave is reflected (from Ratcliffe, 1970).	36
3.5	The absorption process. Electrons (small dots) receive energy from the wave and collide with neutrals (large circles) (from Ratcliffe, 1970).	37
3.6	Typical mid-latitude winter MUFs and LUFs as a function of local time (from USAF Air Weather Service Pamphlet 105-36, February, 1975).	42
3.7	Model vs. Störmer Geomagnetic Cutoffs. Both are valid near geomagnetic local midnight (from Reid and Sauer, 1967).	48
3.8	Penetration of protons and electrons, and cutoff latitudes as functions of velocity (from Hargreaves, 1979, after Bailey, 1959).	49

3.9	IMF-Magnetosphere connection model (from Van Allen <i>et al.</i> , 1971).	52
3.10	Comparison of absorption at 30 MHz (Mc/s) for magnetic conjugates. During daylight hours at Mirnyy (solar elevation $> 0^\circ$), absorption is essentially equal to the Spitsbergen value. Otherwise, values are much lower than at the continuously daylit station (from Gillmor, 1963).	55
4.1	Major stations and physical features in Antarctica. The cross in the lower right quadrant denotes the approximate location of the south geomagnetic pole (from NSF, 1984).	59
4.2	Invariant latitudes near South Pole Station. This is also how the South Pole IRIS is oriented.	60
4.3	Ionospheric projection of IRIS beams (from Detrick and Rosenberg, 1990).	65
4.4	IRIS Quiet Day Curves for October 1989.	66
5.1	Frequency response function of a low-pass filter for $n = 13$, $n = 30$, and $n = 40$, $\Delta t = 1$ min, $f_{c1} = 0$, $f_{c2} = 0.1$, such that oscillations with periods less than 10 minutes ($\Delta t / (f_{c2} - f_{c1})$) will be filtered out.	71
5.2	Near-earth soft x-ray and energetic particles recorded by GOES-7, 19 October 1989 (from <i>Solar Geophysical Data prompt reports</i> , NOAA, November, 1989, Part 1).	75
5.3	South Pole H-, D- and Z-sensor traces, 19 October 1989.	77

5.4	Filtered absorption plots in center column of the IRIS array for the period 1200–2400 UT, 19 October 1989.	78
5.5	Lags corresponding to the maximum cross-correlation ($L_{r_{max}}$) with beam (0,0) for the following periods: a) 1225–1250 UT; b) 1300–1330 UT; c) 1330–1600 UT; and d) 1430–1500 UT, 19 October 1989. The period 1630–2000 UT is not shown because $L_{r_{max}} = 0$ for the entire array.	80
5.6	Filtered data plots of IRIS beams (3,-1), (0,0), and (-3,-1) including the period 1225–1250 UT (Period 1), 19 October 1989.	82
5.7	Lags corresponding to the maximum cross-correlation ($L_{r_{max}}$) with beam (0,0) for the periods 1415–1515, 1420–1520, and 1425–1525 UT, 19 October 1989.	84
5.8	Lags corresponding to the maximum cross-correlation ($L_{r_{max}}$) with beam (0,0) for the period 1437–1507 UT, 19 October 1989.	85
5.9	Collection of correlograms for the period 1437–1507 UT, 19 October 1989.	87
5.10	Filtered IRIS data plots in the middle column for the period 1415–1515 UT, 19 October 1989.	88
5.11	Lag in seconds relative to the center beam for the absorption peak occurring near 1447 UT, 19 October 1989.	90
5.12	Imaged IRIS data for 19 October 1989, 1420–1520 UT.	91
5.13	The polar dayside cusp relative to local geomagnetic time (from Meng, 1981).	94

Chapter 1

Introduction

Solar flares eject energetic particles into interplanetary space. As these particles approach earth's magnetosphere they gain prompt access to the polar ionosphere where geomagnetic field lines are open to space. Occasionally, a flare will introduce particles of sufficient energy to penetrate to the polar D-region, where they finally lose their kinetic energy through ionization of upper atmospheric constituents. Consequently, radio waves transiting polar regions experience partial to total signal attenuation or 'blackout', depending on the magnitude of the event and radio frequency. This phenomenon, which may last several days, is generally confined to high latitudes, hence the term *polar cap absorption* or PCA.

A PCA event is generally believed to start near the geomagnetic poles, eventually expanding to cover the area bounded by the auroral oval. Once in progress, any change in magnitude of the event is believed to occur simultaneously

in the affected region, in direct response to local changes in energetic particle flux.

The most widely used instrument for measurement of radiowave absorption is the *riometer* (relative ionospheric opacity meter). Riometers continually monitor galactic radio sources at a specific frequency channel. These sources are essentially constant and fixed in space (at least for our concerns), so a *quiet day curve* may be computed based on diurnal and seasonal variations brought about by the earth's rotation and orbit, respectively. When D-region ionization is above normal levels, signal strength will be below its quiet day curve value due to absorption by the additional electrons. The magnitude of the PCA at a particular station depends on the ratio of the actual signal to the expected or quiet-day signal.

Until the advent of IRIS (Imaging Riometer for Ionospheric Studies), riometers were merely single broadbeam receivers capable of recording only one value at a given time to represent the absorptive qualities of the overhead ionosphere. The IRIS system, however, employs a 7×7 array of narrow beams, each capable of monitoring a portion of the radio sky. As a result, IRIS allows us to 'image' absorption characteristics and study variations within the instrument's field of view.

A PCA event is merely an ionospheric response to solar proton events; however, analysis of this response is a means of remotely sensing the behavior of particles in the near-earth environment. Our ability to image the ionosphere's response may provide further clues regarding particle energies and energy spectra involved, as well as the local characteristics of earth's magnetic field. If, through

using IRIS, we can detect a delay of effects from one portion of the array to another, this implies a local variation in the ability of energetic protons to penetrate to D-region altitudes.

With this purpose in mind we intend to examine various time periods during the onset and intensification of a PCA event which began on 19 October 1989 to determine whether features in the absorption time series occur simultaneously, or whether there is a tendency for delay of certain absorption features within the field of view.

First, we will briefly discuss energy sources involved and the means for propagation of this energy to the near-earth environment.

Chapter 2

Solar Protons and Their Earthbound Journey

2.1 The Sun and Solar Flares

A detailed discussion of the solar flare process, frequency of occurrence, and relationship to the 22-year solar cycle is well beyond the scope of this thesis. However, a brief description of flares will help understand the source of energy involved in producing near-earth effects such as the PCA.

A solar flare is a cataclysmic release of energy stored in tight magnetic fields (hundreds of gauss) near sunspots. This energy is believed to be released via a rapid annihilation or rearrangement of field lines above complex spot groups. There is no widespread agreement on the exact set of circumstances required to trigger flares or to fully explain their morphology. Svestka (1976) discusses

and critiques several theories. One simple model is illustrated in Fig 2.1. In this model, a magnetic neutral point exists above a pair of spots with opposite polarity. When the field collapses, particles become energized and are drawn away from the neutral point along the reestablished field lines; some are ejected outward to space, and some are drawn back inward, eventually being slowed down and stopped by denser chromospheric gases producing 'hard' (.5-4.0Å) x-rays. The electrons also ionize chromospheric hydrogen, which upon recombination emits H α (centered at 6563Å), soft x-rays (1-8Å), and ultraviolet light (Piddington, 1969).

The most energetic solar flares release most of their energy within the first few minutes, followed by a relatively slow decline to background level lasting from tens of minutes to a few hours depending on flare intensity. The total energy emitted during a flare is something on the order of 10^{25} J (Stix, 1989). This total energy can be divided into two classes: electromagnetic radiation and *corpuscular radiation*, kinetic energy of protons, electrons, and α -particles which exceed solar escape velocity and become part of the solar wind streaming outward into interplanetary space.

Flares are usually classified by their observed size in H α , brightness in H α , and soft x-ray emission but may also be classified according to their radio burst signatures, resulting from the acceleration of energetic particles within the corona. All of these are part of the electromagnetic mode of energy release. A flare's radio signature serves as its fingerprint and is an important consideration when forecasting near-earth particle events. For example, in the context of solar

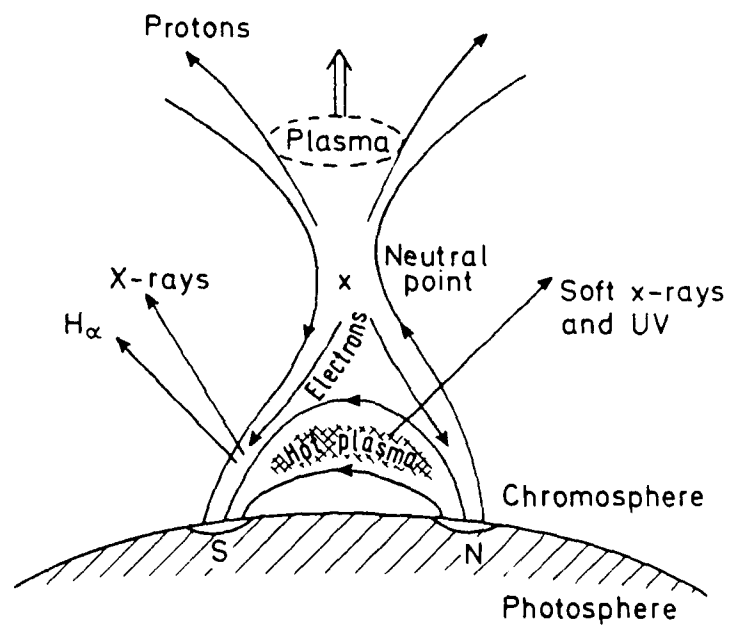


Figure 2.1: A solar flare model, showing possible sources for some known flare products (from Hargreaves, 1979, after Piddington, 1969).

proton events and PCA, Kundu and Haddock (1960) found a high degree of correlation between Type IV bursts [long-lived, smooth, and intense radio bursts covering the 300-30 MHz frequency range, beginning ~20 minutes after flare maximum (SESC, 1988)] and PCA occurrences. Castelli *et al.* (1967) found that a particular U-shaped frequency vs. intensity for Type IV bursts indicates flare ejecta rich in energetic protons; this is now a major PCA forecasting criterion in use at geophysical alert centers.

Corpuscular radiation will receive most of our attention, specifically high-energy protons; however, enhanced x-ray emission also has consequences within the ionosphere, and radio noise storms can contaminate measurements of ionospheric radiowave absorption, as will be discussed in a later chapter. For now, we'll follow the energetic particles on their journey earthward.

Figure 2.2 diagrams the near-earth effects of a solar flare; many of the phenomena will be discussed in later sections.

2.2 Travel of Plasma Through the Interplanetary Medium

Energetic particles in the presence of a magnetic field spiral around field lines as a result of the Lorentz force, $F = q(\vec{v} \times \vec{B})$, for a particle of charge q and velocity \vec{v} in a magnetic field of inductance \vec{B} . Particle gyro-radius is given by $r_B = mv_{\perp}/qB$, where m is particle mass and v_{\perp} is the magnitude of \vec{v} perpendicular to \vec{B} .

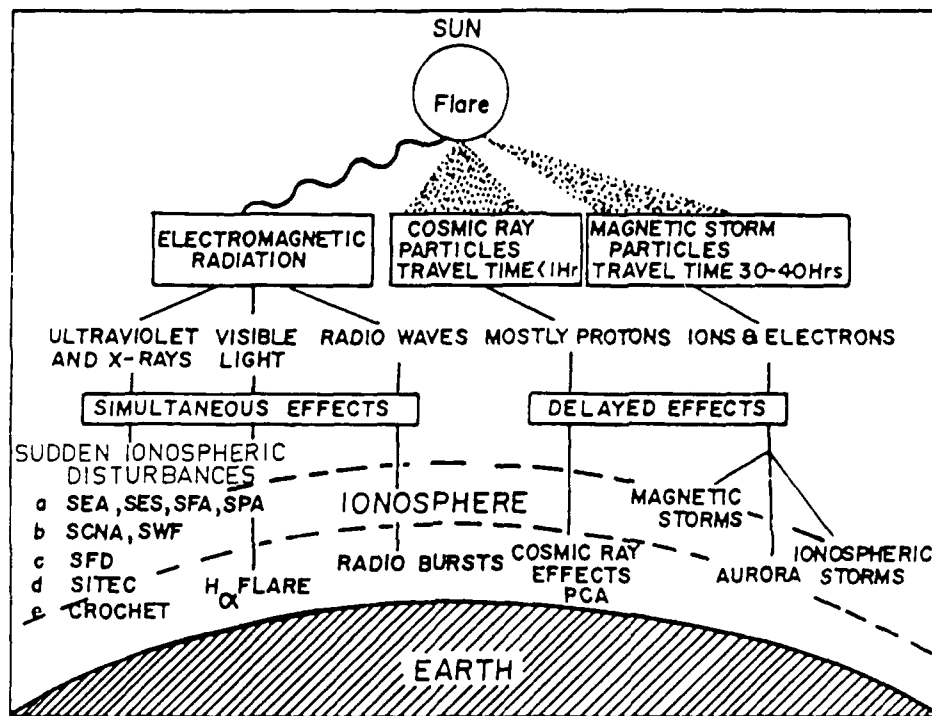


Figure 2.2: Diagram of solar flare products and near-earth effects (from Mitra, 1974).

Due to the extremely high conductivity of plasma, particles are constrained or 'frozen-in' to a particular field line; therefore, particles do not travel across field lines, and two magnetized plasmas brought together cannot mix unless their respective field lines merge together. Furthermore, if plasma energy density (particle energy per unit volume) is greater than magnetic field energy density, motion of the plasma will carry the magnetic field line with it. Conversely, if magnetic energy density dominates, the magnetic field will control movement of particles within the plasma (Hess, 1965; Townsend *et al.*, 1982).

With this background, we now briefly discuss the environment encountered by energetic particles of solar origin as they propagate into interplanetary space.

2.2.1 The Interplanetary Magnetic Field (IMF) and The Solar Wind

Within about 1 solar radius of the solar 'surface,' regions exist where the magnetic energy density dominates and plasma are trapped by the field. Farther out into the solar corona, magnetic energy density begins to decrease faster than that of the plasma, and at about $3 R_{sun}$, the plasma energy density dominates. Thus, the escaping plasma carries the field lines outward into the interplanetary medium forming what is known as the *interplanetary magnetic field* (IMF). This outward streaming of plasma is termed the *solar wind*.

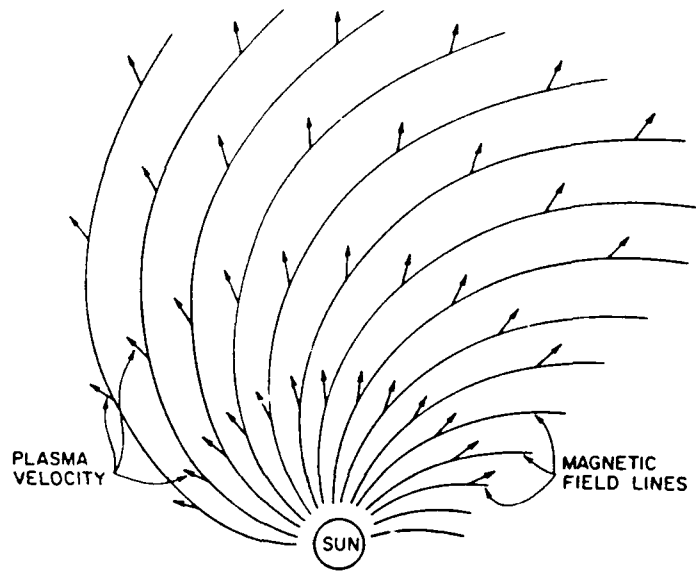
Since magnetic energy dominates near the sun, inner coronal mass will rotate with the sun, which has a rotation period on the order of 27 days; however,

escaping plasma is no longer constrained. Therefore, it will lag behind its point of origin at the sun, causing an Archimedes spiral orientation of magnetic field lines as shown in Fig 2.3. This spiralling motion is also referred to as the *garden hose effect*, where a water jet source is spinning, resulting in a spiral jet configuration, while the individual water drops are actually moving radially. At 1 AU, the angle between the field lines and the radial or sun-particle position vector is $\sim 45^\circ$ (Townsend *et al.*, 1982).

As a consequence of the spiral effect, the favored source region for PCA-producing flares is west of central meridian (the west limb is defined as the leading edge of the disk as it advances across the sky from an earth observer's perspective) (Obayashi and Hakura, 1960). For the same reason, a solar proton event may also result from a flare occurring just behind the west limb, hidden from our vantage point on earth.

The solar wind is merely an extension of the solar corona, consisting of electrons, protons (hydrogen nuclei), and α -particles (helium nuclei). This stream is a permanent feature, although its velocity and density are highly variable depending upon the level of solar activity. Velocities normally fall within the range of 200–700 km s⁻¹, with 'gusts' of minutes to a few hours duration. On average, particle density is around 6.5 cm⁻³, but can be as little as 0.4 cm⁻³ during solar minimum to as much as 100 cm⁻³ during solar maximum (Bruzek and Durrant, 1977).

(a) STATIONARY FRAME OF REFERENCE



(b) ROTATING FRAME OF REFERENCE

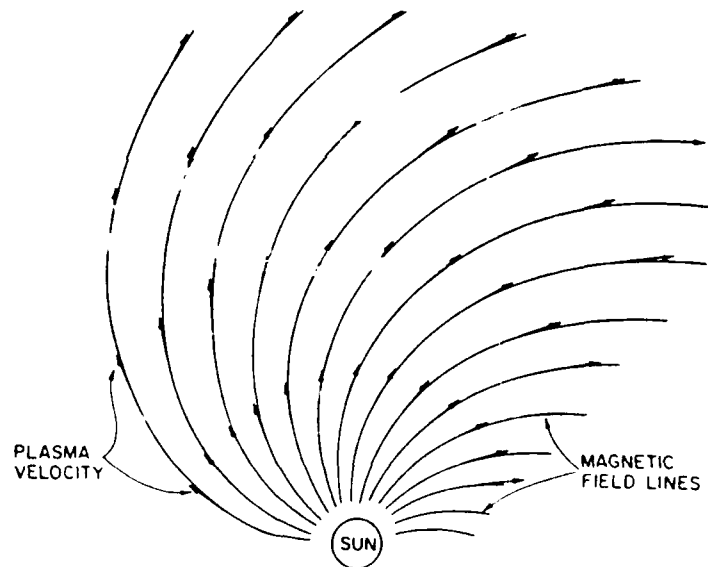


Figure 2.3: Archimedean spiral structure of the IMF in (a) stationary reference plane and (b) rotating with the sun, showing plasma flow and magnetic field structure (from Hundhausen, 1972).

2.2.2 The Neutral Sheet

Near the sun's equatorial plane, observations have shown that the magnetic field is organized into *sectors*, regions where the field lines are predominantly directed either sunward or antisunward along the spiralling IMF. The sector boundary separating fields of opposite polarity is quite thin and may be swept past earth in a matter of hours, whereas the sector itself may take on the order of one week to sweep past earth. A *neutral sheet* separates plasmas which flow from the sun's northern and southern hemispheres, which have oppositely directed magnetic fields. The neutral sheet can be visualized as an extension of the heliomagnetic equator into space (see Fig 2.4) (Townsend *et al.*, 1982).

Since the neutral sheet's photospheric footprint (*i.e.*, the neutral line at the sun where the north-south polarity reversal occurs) can be displaced meridionally, the current sheet can likewise become warped as shown in Fig 2.5, and earth will occasionally cross from one sector to another. Consequently, the position of earth relative to the neutral sheet will determine whether or not it is susceptible to energetic particles. For example, energetic particles emanating from a flare in the northern heliomagnetic hemisphere tend to remain on the northern side of the neutral sheet. If earth is south of the current sheet when the particles reach 1 AU, it will be shielded from the particles. If earth lies on the same side, near-earth effects are possible.

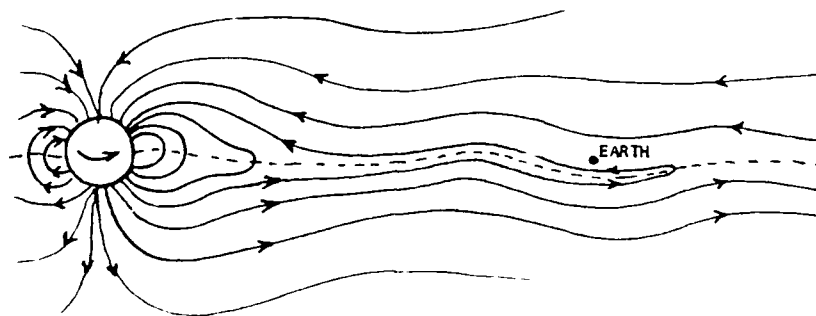


Figure 2.4: Formation of a neutral sheet. Earth is pictured above (north of) the sheet (from Townsend *et al.*, 1982).

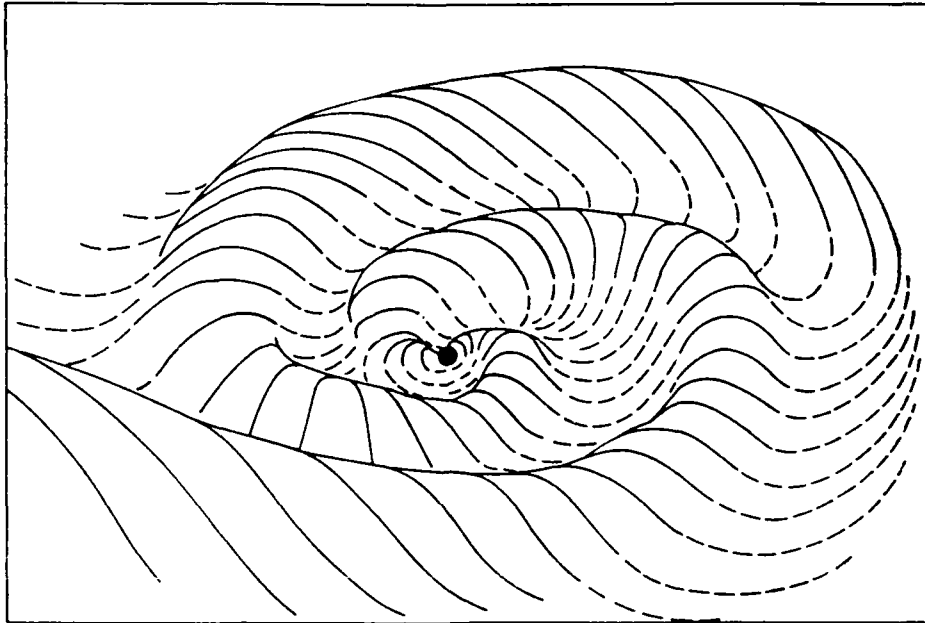


Figure 2.5: Warped neutral sheet; solid (dashed) lines lie above (below) ecliptic plane (from Bruzek and Durrant, 1977).

2.3 Interaction with the Magnetosphere

As the solar wind approaches earth, it encounters an obstacle, namely earth's *magnetosphere*, the volume within which earth's magnetic field dominates the motion of charged particles. Before discussing the coupling between the IMF and the geomagnetic field, a general description of the magnetosphere is in order.

2.3.1 Structure of the Magnetosphere

A simplified diagram of the magnetosphere is shown in Fig 2.6. Most of the material in this subsection is paraphrased from Bruzek and Durrant (1977).

The *magnetopause* is the surface where solar wind particle pressure balances geomagnetic field pressure. On the dayside, this surface is, on average, situated at 10–12 R_e ; however, for a particularly fast or dense solar wind, this may be reduced to 6–9 R_e . On the night (anti-sunward) side, the magnetopause extends back an estimated 1000 R_e (SESC, 1988), encasing the *geomagnetic tail* or *magnetotail*, where geomagnetic field lines are drawn back by the motion of the solar plasma.

As shown in Fig 2.6 the field lines in the northern tail lobe are directed toward the earth and those in the southern lobe are directed away from the earth. The transition region between the northern and southern lobes defines the *neutral sheet*, which begins about 10 R_e and extends back into the magnetotail. The neutral sheet consists of electrons and protons with number densities ~ 0.1 – 0.3 cm^{-3} , electron energies ranging from 200 eV to 12 keV, and proton energies

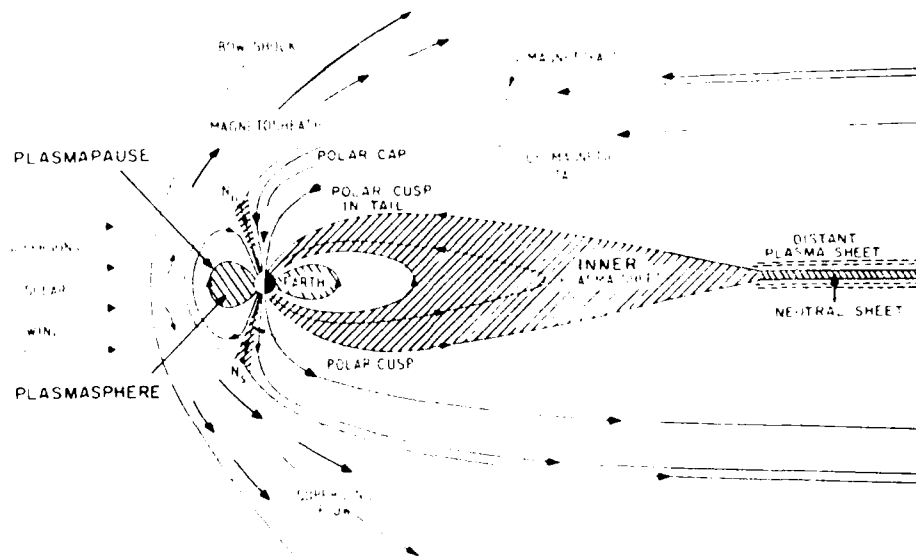


Figure 2.6: A magnetospheric model (from Bruzek and Durrant, 1977).

from 1 to 20 keV.

Closer to the earth on the nighttime side is the *inner plasma sheet*, consisting of electrons with energies ~ 0.5 to 2 keV and protons with energies ~ 2 to 10 keV. Typical number densities are ~ 0.3 – 1.0 cm^{-3} .

Upstream from the magnetopause is the *bow shock*, analogous to an ordinary aerodynamic shock wave. The bow shock is the boundary between the undisturbed flow of the solar wind and a region of turbulent, post-shock solar wind known as the *magnetosheath*. Here, solar wind speeds have been reduced significantly, becoming heated in the process to approximately 10^6 K .

The narrow region between closed geomagnetic field lines on the sunward side and lines which are swept back into the magnetotail is called the polar *cusp* or *cleft*. The cusp can be thought of as a neutral region or 'funnel' providing direct access to particles within the magnetosheath (see Fig 2.7). Although the terms cusp and cleft are sometimes used interchangeably, cleft implies greater extension in local time; therefore the cleft is more of a wedge than a funnel, as shown in Fig 2.8. Both are located approximately 10 – 15° latitude equatorward of the geomagnetic poles near magnetic local noon (SESC, 1988).

2.3.2 Entry of Solar Energetic Particles into the Magnetosphere

So far, we have discussed the source of those particles which cause near-earth effects, their journey through space, and the obstacle presented by the

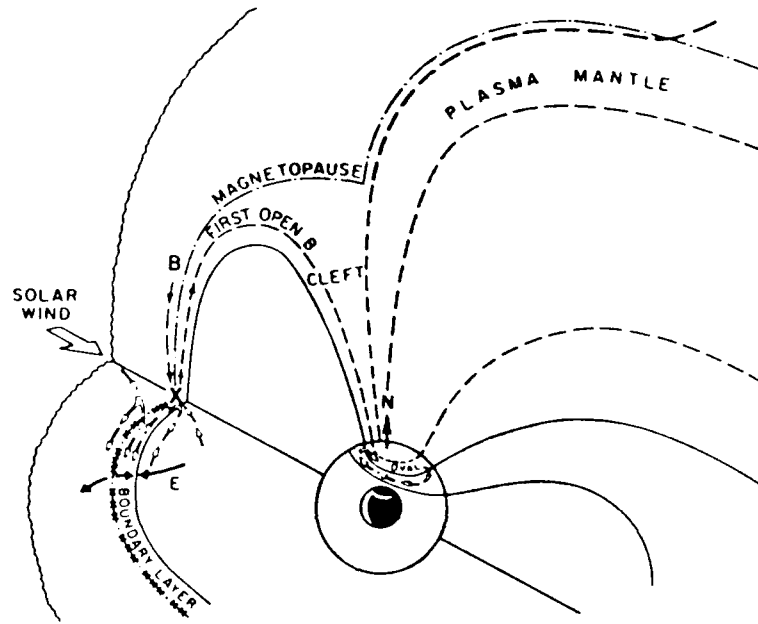


Figure 2.7: Three dimensional view of magnetosheath plasma inside the magnetopause. This diagram depicts an IMF with southward component and shows how the IMF and geomagnetic fields connect on the dayside via X-type reconnection. Notice how field lines map down into the auroral and polar regions (from Heikkila, 1985).

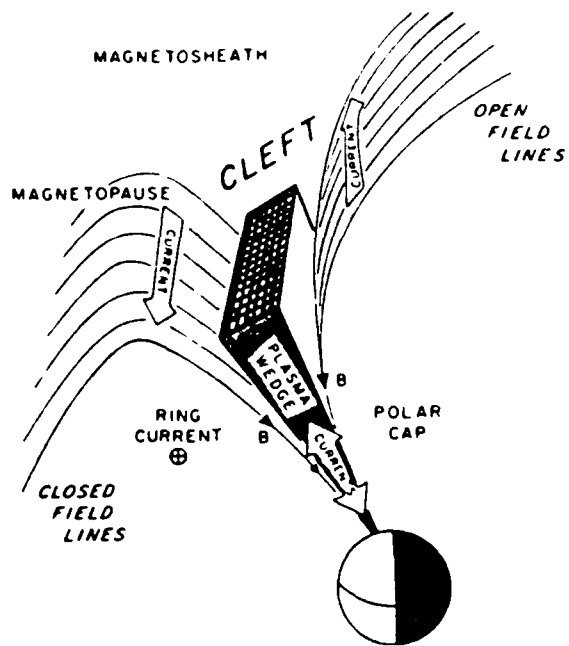


Figure 2.8: The polar cleft, distinct from the cusp in that it has greater extent in local time, whereas the cusp is relatively small and isolated near local noon (from Heikkila, 1985).

magnetosphere. How then, do the particles gain access into the magnetosphere and, ultimately, the ionosphere? First, consider two possible IMF conditions: one with a northward component, one with a southward component.

When the IMF has a northward component, the north-south component of the IMF points toward ecliptic north. Under this condition, the IMF does not easily connect into the geomagnetic field, thus very little interaction or particle interchange takes place. This is the so-called *closed magnetospheric model*. With a southward component, merging or interconnection of IMF and geomagnetic field lines can occur because field lines are oppositely directed on the sunward magnetospheric boundary. It is believed that IMF and geomagnetic field lines merge together via an X-type neutral point on the dayside. Once merged, these lines are dragged back into the magnetotail, where a similar reconnection eventually takes place. Not surprisingly, this is called the *open magnetospheric model* (Dungey, 1961). Both models are shown in Fig 2.9.

The open model can be divided into three regimes, based on the type of field lines encountered: closed field lines, distorted closed field lines, and open field lines. Close to the earth, closed, symmetric magnetic field lines are generally the rule; i.e., both ends connect back to the earth. These field lines generally connect to earth at latitudes up to $\sim 60^\circ$. Poleward of the closed lines are the distorted closed lines. On the sunward side they extend out along the magnetopause, and on the night side, they pass through the current sheet, and are separated from the symmetric closed lines by what is called the *polar cusp in tail* or *plasma cusp*, different from the polar cusp discussed earlier. Finally, further poleward

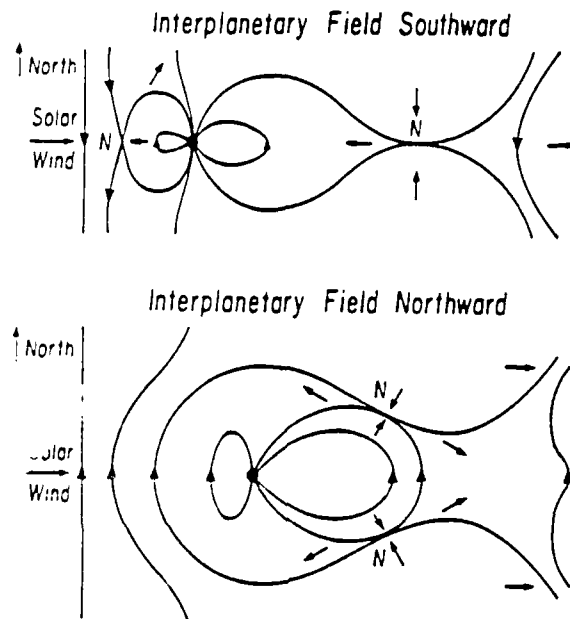


Figure 2.9: Dungey reconnection model for southward and northward IMF. X-type neutral points are labelled *N*, and arrows denote motion of field lines during the reconnection process (from Russell, 1987).

are the open field lines, which are either swept back to form the magnetotail or are directly connected to the IMF.

In an open magnetosphere, particles are free to enter the polar caps along reconnected field lines, and clefts allow direct access by solar wind plasma into the dayside auroral zones.

Particles of sufficient *rigidity* may diffuse across field lines. Rigidity is defined as momentum per unit charge and is a measure of the ability of a particle to stray from a particular magnetic field line. Rigidity, P , is related to energy, E , by

$$P = \frac{1}{q} \sqrt{E^2 + 2m_0c^2E} \quad (2.1)$$

where q is the particle's charge, c is the speed of light in a vacuum, and m_0 is the rest mass of the particle (SESC, 1988). The higher a particle's rigidity, the higher its potential for crossing field lines.

So, we now have a mechanism for entry into the magnetosphere. Once inside the earth-magnetosphere system, energetic particles will either be trapped, stored for later deposition into the ionosphere, or immediately deposited in the polar regions.

2.3.3 Trapped Radiation

Within the magnetosphere is a region of trapped radiation known as the Van Allen radiation belts after J. A. Van Allen. These regions of trapped energetic particles, first observed in 1958 (*c.g.*, Van Allen and Frank, 1959; Van Allen *et al.*, 1959) are manifestations of closed geomagnetic field lines. Particles initially

having sufficient rigidity to stray from the weaker field lines at the fringes of the magnetosphere eventually encounter stronger field strengths closer to earth and thus become constrained to a field line.

There are two major trapping regions, aptly named the *inner* and *outer* Van Allen belts (see Fig 2.10).

The outer belt, centered between 3-5 R_e , contains solar wind particles (~ 200 keV-2 MeV) which have diffused across the magnetopause in the magnetotail, and are accelerated earthward during geomagnetic disturbances. On the dayside, this belt extends out to the magnetopause.

The inner belt, centered at $\sim 1.5 R_e$ consists of higher energy (some >30 MeV) protons of terrestrial origin, believed to be created via bombardment of upper atmospheric constituents by extremely high energy particles (galactic cosmic rays). The inner belt is a part of the *plasmasphere*. Between the inner and outer belts, is a region of $<1 R_e$ thickness, where there is a relative minimum in proton density; this region is termed the *slot* and corresponds to the *plasmopause* (SESC, 1988).

2.3.4 Geomagnetic Storms and Aurora

The subject of aurora and geomagnetic substorms is quite actively studied. Countless volumes of material have been written, and doubtless many more have yet to be completed. The focus of this study will not directly broach the subject, but a brief description is important.

Though faint aurora exist even under quiet geomagnetic conditions, bright

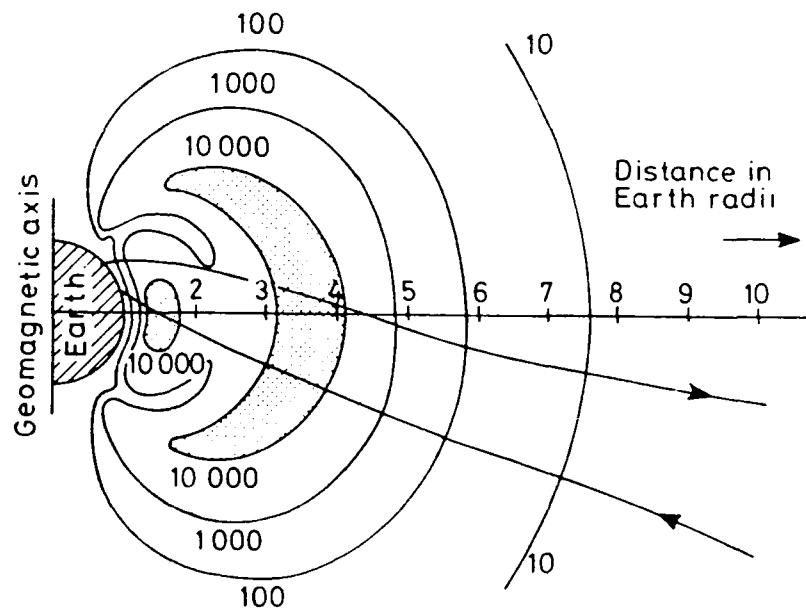


Figure 2.10: Inner and outer radiation belt zones from Pioneer IV. Contours are geiger counting rates. The inner zone consists of high energy (some with $E > 30$ MeV) protons; the outer zone consists of solar wind particles, some in excess of 1.5 MeV (from Hargreaves, 1979, after Van Allen and Frank, 1959).

aurora are actually the result of *geomagnetic disturbances*, defined as 'variations in the geomagnetic field which do not have a simple periodicity and which appear to result from changes in the interplanetary environment' (Townsend *et al.*, 1982). These disturbances are the result of variations in solar wind density and/or speed, which alter the pressure balance between the solar wind and the geomagnetic field at the magnetopause. Alteration of this balance brings about a series of internal adjustments within the magnetosphere eventually resulting in an earthward displacement of the plasma sheet and the injection of charged particles along field lines into the auroral zone. Geomagnetic disturbances may last from a few hours to a couple days.

Numerous indices are used to characterize the local and planetary-scale level of geomagnetic activity. One of the most popular is the K_p index, a 3-hourly value calculated at the Institut für Geophysik der Göttingen Universität, West Germany, from K-indices observed at 13 stations, mostly in the northern hemisphere. The local K-index is a 3-hourly quasi-logarithmic index measuring the most disturbed horizontal magnetic field component. Both indices range from 0 (quiet) to 9 (most disturbed) (SESC, 1988).

Aurora are caused by precipitating low-energy protons and electrons (average energy ~ 6 keV), which spiral down magnetic field lines into the upper atmosphere, where they collide with and give their energy up to ionize neutral atmospheric constituents, namely monatomic and diatomic oxygen and nitrogen. Normally, the lower boundary of this activity occurs at ~ 100 km. Emission is not limited to the visible spectrum: bremsstrahlung x-ray and radio emissions are also

common (Hargreaves, 1979; SESC, 1988). Another effect is *auroral zone absorption* (AZA), caused by penetration of auroral particles into the lower ionosphere, considered later in this study.

Aurora tend to be concentrated in a band near 67° corrected geomagnetic latitude (CGL) at local midnight, and 75° CGL at local noon under average conditions. On the nightside, this *auroral oval* is the intersection of the cusp in tail (discussed earlier) and the ionosphere; on the dayside, it is defined as the intersection of the ionosphere with the dayside cleft. Figure 2.11 shows how the average position of the oval changes during the course of a day relative to South Pole Station.

The zones of maximum occurrence of nighttime aurora as seen by observers at a fixed point on earth are called the *auroral zones*. These are located at about 67° north and south latitude and are $\sim 6^\circ$ wide (Bruzek and Durrant, 1977). Brightening, widening, and equatorward displacement of the oval are all related to geomagnetic storms.

In addition to global scale disturbances, the geomagnetic field exhibits smallscale fluctuations even during magnetically quiet times. These *pulsations* are either continuous and sinusoidal (Pc) or irregular (Pi) in nature. Periods typically range from a few tenths of a second to ~ 10 minutes for Pc, and a few seconds to ~ 2 minutes for Pi (SESC, 1988). Pulsations of this sort are believed to be caused by Kelvin-Helmholtz instability at the magnetopause (see *e.g.* Chen and Hasegawa, 1974).

SOUTH POLE STATION FIELD OF VIEW
RELATIVE TO AURORAL OVAL

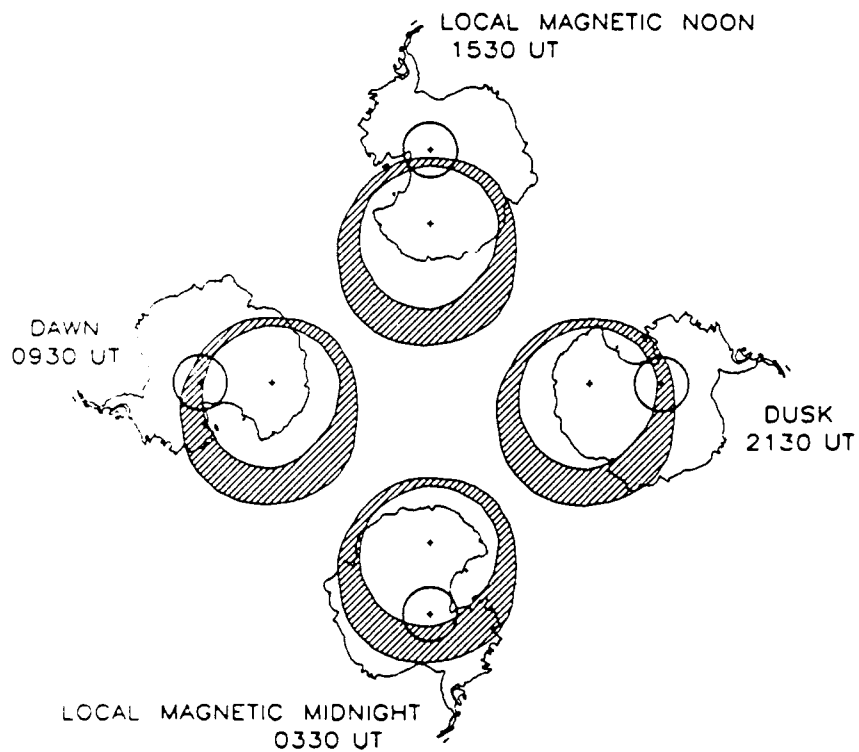


Figure 2.11: Average auroral oval position for various times of the day. The small cross is the south geomagnetic pole; the circled cross is South Pole Station (geographic pole). The solar direction is toward the top of the figure (from Rairden and Mende, 1989).

Chapter 3

The Ionosphere

We come now to that region of the earth's atmosphere made up of free electrons and protons produced by photodissociation of upper atmospheric constituents and precipitation of energetic particles. Since its discovery, the *ionosphere* has been divided into a series of regions or layers defined as relative maxima in the vertical particle density profile. These layers are quite variable, depending on the level of solar activity and the solar zenith angle (thus season, latitude, and time of day). Furthermore, there are no definite boundaries between layers or regions; in fact, the D-region virtually disappears at night under quiet conditions. The day versus night variation for different levels of solar activity is shown in Fig 3.1.

Briefly, we will discuss the formation of these layers and the characteristics of the E and F layers before concentrating on the D-region, the primary focus of this study.

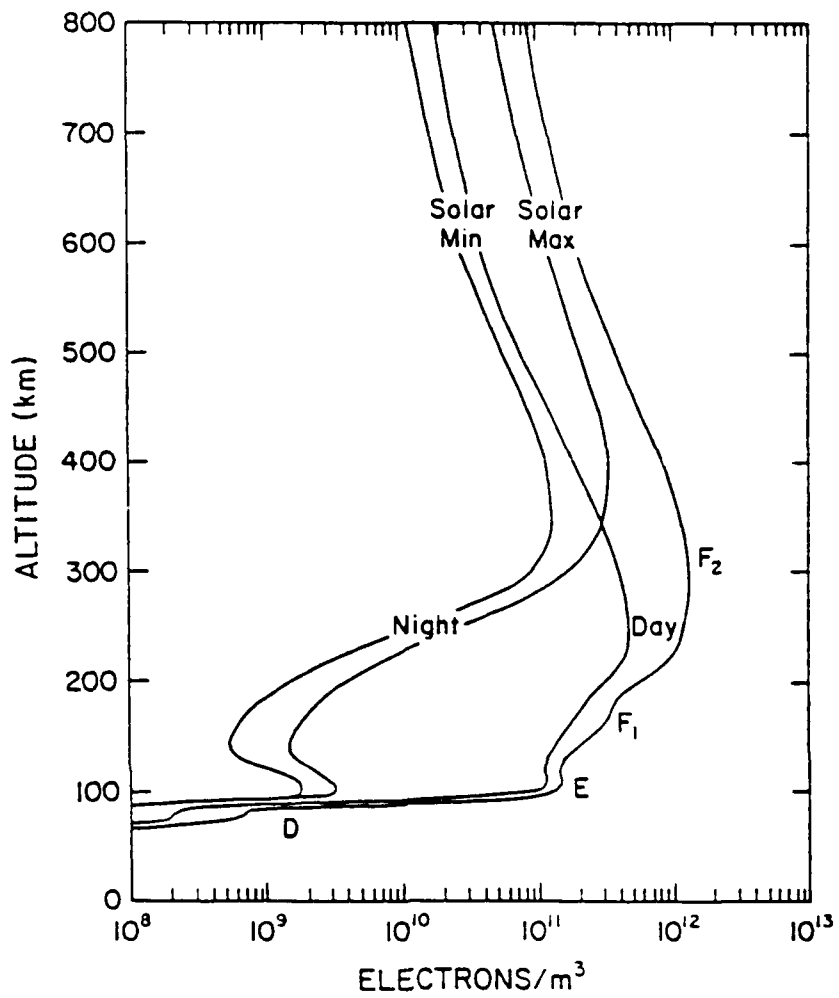


Figure 3.1: Typical midlatitude ionospheric electron density profiles during solar maximum and minimum, day and night. Different altitude regions are labeled *D*, *E*, *F*₁, and *F*₂ (from Richmond, 1987).

3.1 Ionospheric Layers and Chapman Theory

In 1931, Sydney Chapman theorized the formation of layers based on the premise that for monochromatic radiation in an isothermal, stably-stratified atmosphere, maximum ionization would occur at the altitude of maximum absorption, assuming the ionized gas is the only absorbing constituent. Without deriving the Chapman production function, we can describe what is going on by referring to Fig 3.2.

As radiation (I_λ) enters the atmosphere, it initially encounters low molecule number densities (ρ_m), so that the potential for ionization is low. Penetrating deeper into the atmosphere, the nearly exponential increase in number densities results in increased ionization (q_e); however, monochromatic intensity is being decreased exponentially. In the lower atmosphere, number densities are high, but radiation intensity has been reduced so that ionization again tapers off. This profile only explains the profile yielded due to one gas at one specific frequency. Each gas will have a different profile at a given frequency.

The same basic argument is true of ionization due to precipitating energetic particles, whose atmospheric penetration depth is a function of their kinetic energy (rigidity).

3.1.1 The E-Region

The E-region lies roughly between 90 and 160 km, with a maximum number density near 105 km; these heights are dependent on solar zenith angle and

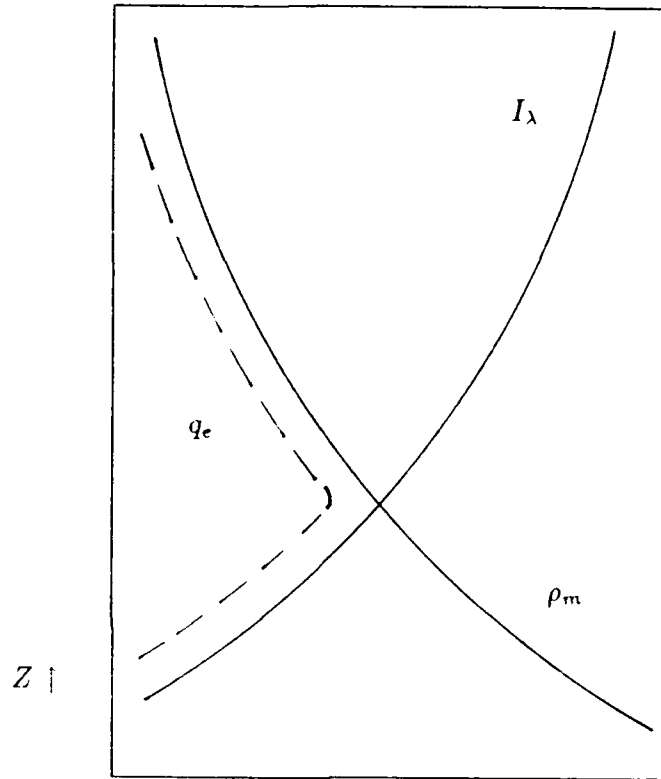


Figure 3.2: Chapman layer formation process, where q is ion production rate, I_λ is the specific intensity of ionizing radiation, and ρ_m is neutral particle density.

level of solar activity. Ionization is achieved mainly by daytime interaction of x-rays (8-104Å) and EUV (800-1026Å) with O_2 forming O_2^+ and e^- . X-rays ionize N_2 and monatomic oxygen as well; but x-ray flux is dependent on solar activity, and quite small during solar minimum (Hargreaves, 1979).

3.1.2 The F-Region

Above the E-region is the F-region, which is composed of two subregions, denoted F1 and F2. In the F1 region, (~140-200 km), EUV in the 200-910Å range chiefly ionizes monatomic oxygen, with some contribution from ionization of N_2 . During the nighttime, since ionizing radiation is gone, the F1 layer merges with the F2 layer. The F1 layer is the primary production layer in the ionosphere. The F2 layer (~200-600 km) is quite complex and different from other ionospheric regions in that no significant ionization occurs within the layer; it is fed from F1 layer during the daytime and from the plasmasphere at night (Townsend *et al.*, 1982). Of all the ionospheric regions, the F2 layer exhibits the highest response to changes in solar activity and is quite seasonally dependent. It is also the most important region within the context of long-distance radiowave propagation, to be discussed in a later section.

3.1.3 The D-Region

Lying below the E-region between 50 and 100 km is the D-region. Except in the polar ionosphere, this is essentially a daytime-only region, since normal ionization is principally due to solar x-ray (1-8Å), Lyman- α (1215Å), and EUV

(1027-1118Å) ionization of O_2 and N_2 , NO , and O_2 , respectively (Chamberlain and Hunten, 1987). In polar regions and the auroral zone, almost continual particle precipitation enhances the electromagnetic solar effect during the day and provides at least a trace of ionization during nighttime hours.

3.2 Ionospheric Radiowave Propagation

3.2.1 Ionospheric Refraction of Radio Waves

As a consequence of ionospheric layers or regions, we are capable of exploiting the ionosphere to communicate long-distance using radio waves. Consider a train of radio waves entering a medium from below, so that electron density within the medium increases with height. Snell's Law states that

$$\mu_o \sin \theta_o = \mu_1 \sin \theta_1 \quad (3.1)$$

where θ_o is the original angle from vertical, θ_1 is the angle from vertical in the medium, μ_o is the index of refraction prior to entering the medium, μ_1 is the index of refraction within the medium. For a given angle of incidence, and neglecting magnetic field and collision effects,

$$\mu = \sqrt{1 - k \frac{N_e}{f^2}} \quad (3.2)$$

where k is a constant, N_e is the electron number density, and f is the signal frequency (Davies, 1966).

As we go higher and higher into the increasingly dense medium, μ decreases and θ_o increases, so the signal is bent farther from the vertical (see Fig

3.3). We also see from (3.2) that the effect of increasing frequency is to decrease the bending.

Let us now consider a packet of waves to have some cross-sectional area or *wave front*. Since the phase velocity, V_p , is given by $V_p = c/\mu$, the upper edge of the wave front will have a greater phase velocity than the lower edge, causing a downward bending of the wave. See Fig 3.4 for this phenomenon, known as *Huygens' Principle*.

This is the fundamental reason why a given signal may reflect from an ionospheric layer. We now turn our attention to a special case of signal attenuation, namely absorption.

3.2.2 Absorption

Radiowave absorption occurs when the wave imparts energy to free electrons, causing them to bounce off neutral atmospheric constituents in random directions (see Fig 3.5). Thus the ordered energy received from the wave is converted to disordered, random energy. In the process, the electrons are heated; eventually, this heat energy is passed on to heavier neutral constituents. In theory, a broadcast radio transmitter can increase electron temperatures in the D-region by ~ 45 K (Ratcliffe, 1970).

Neglecting magnetic field effects, the absorption coefficient κ (absorption per unit length) of a radio wave can be expressed as

$$\kappa \propto \frac{1}{\mu} \frac{N_e \nu}{(f^2 + \nu^2)} \quad (3.3)$$

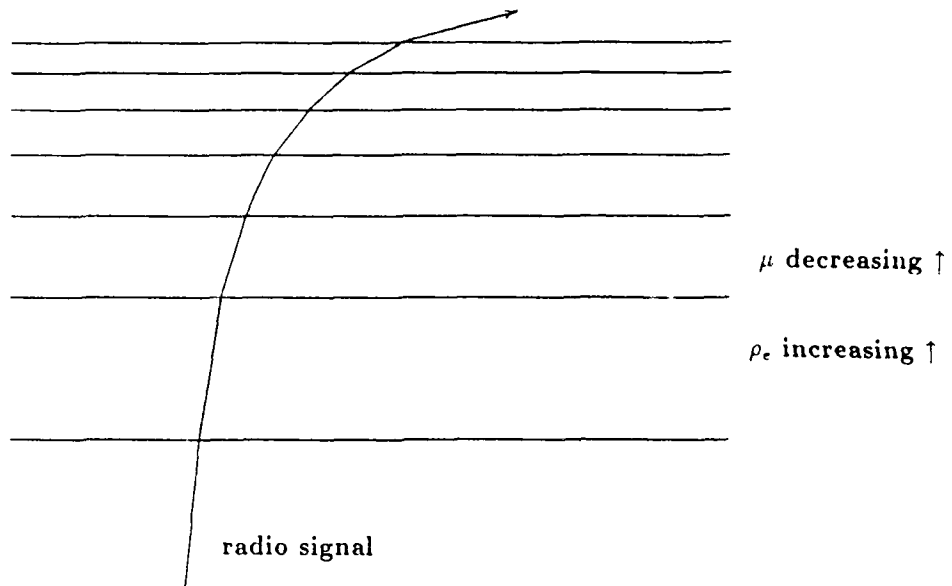


Figure 3.3: Application of Snell's Law to a stratified medium where electron density is increasing with height.

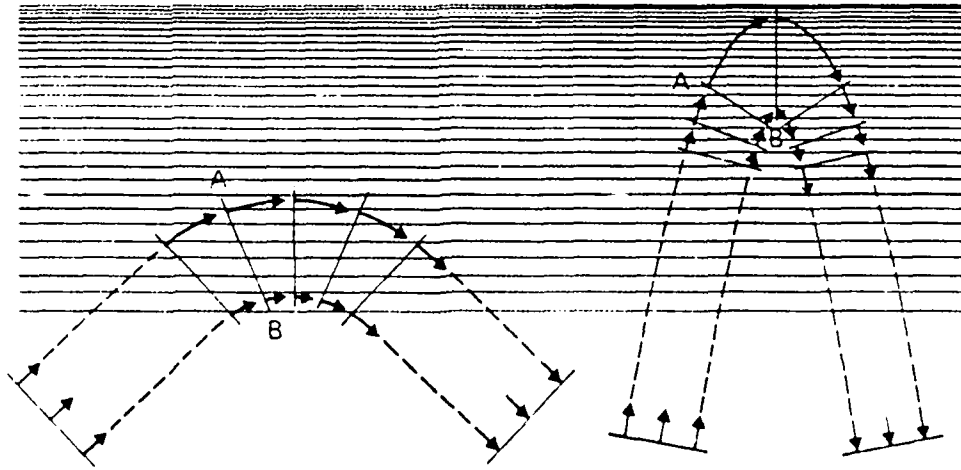


Figure 3.4: A wave approaching a layer of charged particles from below. The concentration of charged particles increases upward. Since μ decreases upward and $V_p = c/\mu$, the top of the wave (A) travels more rapidly than the bottom (B) so the wave is reflected (from Ratcliffe, 1970).

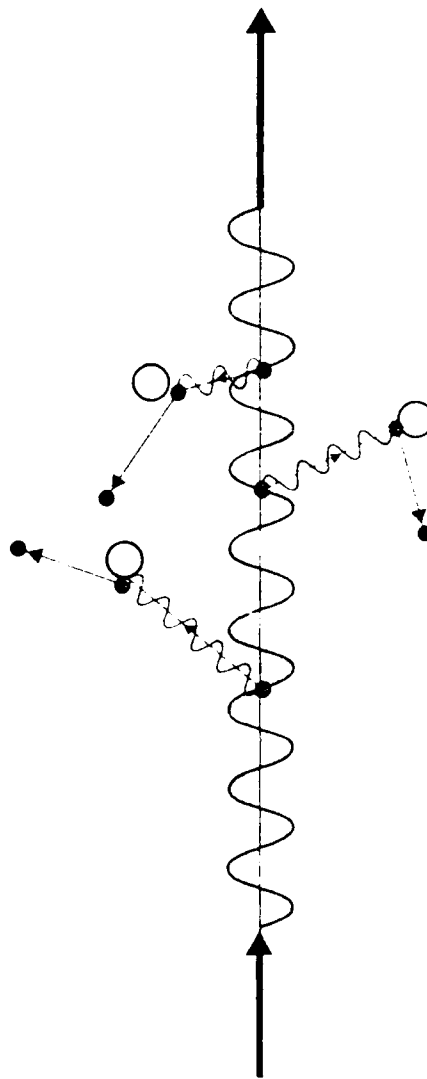


Figure 3.5: The absorption process. Electrons (small dots) receive energy from the wave and collide with neutrals (large circles) (from Ratcliffe, 1970).

where N_e is electron density, ν is collision frequency, and f is signal frequency (Davies, 1966).

In the context of radiowave propagation, absorption can be divided into two categories: *deviative* and *non-deviative*. Deviative absorption dominates where significant refraction occurs (*e.g.*, near the peak density of the F-layer, where $\mu \ll 1$) and refers to path line variation. For deviative absorption, κ is expressible as

$$\kappa_{dev} \propto \nu \left(\frac{1}{\mu} - \mu \right) \quad (3.4)$$

Notice that deviative absorption does not depend on frequency (Davies, 1966). Non-deviative absorption refers to absorption along a straight line path. This occurs when $\mu \simeq 1$ and when the product $N_e \nu$ is large. Collision frequency, ν , is proportional to the density of neutral constituents, which decreases exponentially with height. Electron density, N_e , increases up to the F2 layer. The product $N_e \nu$, and therefore absorption, is a maximum within the D-region (Goodman and Uffelman, 1984). For non-deviative absorption, when $\nu \ll f$,

$$\kappa_{nondev} \propto \frac{N_e \nu}{f^2} \quad (3.5)$$

When $\nu \gg f$,

$$\kappa_{nondev} \propto \frac{N_e}{\nu} \quad (3.6)$$

so that increasing collision frequency decreases non-deviative absorption. The latter relation applies to VLF and LF waves, as we will discuss in the next section.

The presence of a magnetic field complicates matters by introducing *ordinary* and *extraordinary* wave modes resulting from changes in refractive index due to ion gyro-motion about magnetic field lines. The general expression in this case becomes

$$\kappa \propto \frac{N_e \nu}{(f \pm f_H)^2 + \nu^2} \quad (3.7)$$

where f_H is gyrofrequency, given by

$$f_H = \frac{Bq}{2\pi m} \quad (3.8)$$

for a particle of mass m and charge q in a magnetic field of inductance B . The ordinary wave corresponds to the (+) case and the extraordinary wave corresponds to the (-) case for $f \pm f_H$. Thus, the ordinary wave will suffer less absorption, in general, than the extraordinary wave in the presence of a magnetic field. Notice that f_H is independent of particle velocity. In the ionosphere, a typical value for f_H is ~ 1.4 MHz. As signal frequency increases, the relative importance of f_H diminishes, and since we will discuss a system at 38.2 MHz, we will neglect this effect (Hargreaves, 1979; Davies, 1966).

3.3 Enhanced D-Region Ionization

Owing to the high density, and thus the availability of molecules for ionization, the D-region is particularly responsive to sudden changes in electromagnetic fluxes resulting from solar flares. Likewise, high-energy particles ejected by a flare are likely to penetrate to D-region altitudes contributing to enhanced ionization

not only on the dayside, but on the nightside as well. Enhancements due to electromagnetic and corpuscular radiation anomalies tend to result in ionization at lower altitudes, lowering the effective height of the D-region. The effect of these D-region anomalies on radiowave propagation is a function of frequency, angle of incidence, and transmitted power.

At VLF (3–30 kHz) and LF (30–300 kHz), the D-region acts as a reflecting layer. Therefore a change in effective height of this reflector will alter the geometry of the propagating signal, resulting in a change of path length and transmission time. Since VLF and LF are important tools for navigation, submarine communication, and aircraft direction-finding, any unexpected D-region anomaly may have disastrous results.

The medium frequency (MF) band (300–3000 kHz) includes commercial AM broadcast bands. Except at the lower frequency end, the D-region generally absorbs these frequencies, so that during the day, successful propagation is generally restricted to the *ground wave* mode. At night, when the D-region vanishes (except in polar regions), signals may be reflected from the E or F2 regions, dramatically increasing the range. Therefore, only a nighttime D-region anomaly, namely ionization due to particle precipitation, will affect MF transmissions significantly.

Long-distance propagation of HF (3–30 MHz) transmissions is generally achieved via refraction within the E and F regions. The signal must be of high enough strength and frequency (since $\kappa \propto \frac{1}{f^2}$) to pass through the D-region, reflect from the E or F2 layer, then pass through the D-region again to the

receiver site. The minimum frequency for a given time and angle of incidence is called the *lowest usable frequency* (LUF). However, unless the signal is less than some critical frequency, it will pass through the E and F-layers into space. For a signal travelling vertically, this critical frequency is given by

$$f_{crit}(Hz) \simeq 9\sqrt{N_{max}} \quad (3.9)$$

where N_{max} is the peak electron density (m^{-3})(Richmond, 1987). This upper threshold for a given time and angle of incidence is the *maximum usable frequency* (MUF). A typical trace for a mid-latitude path for a 24-hour period is illustrated in Fig 3.6. Notice that both the MUF and LUF reach maxima at midday. This is the effect of daytime ionization in the D and F regions. The key point is that when D-region ionization increases, the LUF also increases, thus decreasing the window of usable frequencies. Both MUFs and LUFs increase with the angle between the slant path and solar zenith angle, since in a slant path the signal will encounter more ionized molecules than in a vertical path.

Other than saying that the lower VHF (30-300 MHz) behaves like HF with respect to D-region effects, we will not discuss higher frequencies, such as UHF and SHF. From here on we wish to limit our discussion to HF and lower VHF frequencies since these are the observational frequencies of the absorption measuring systems used in the present study.

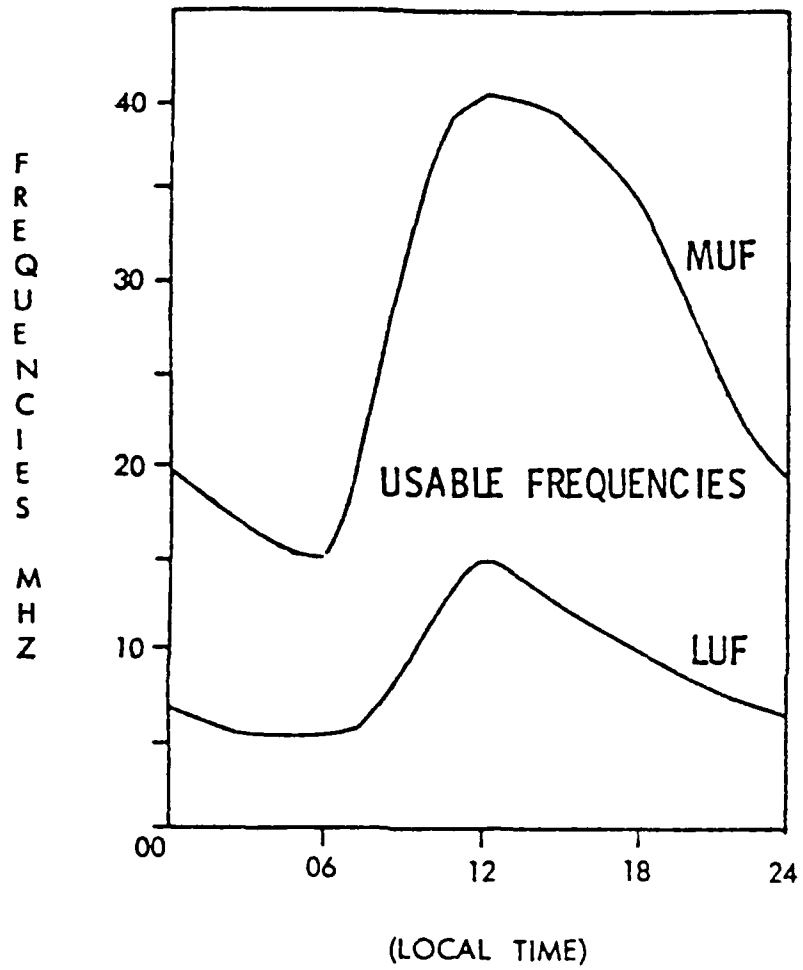


Figure 3.6: Typical mid-latitude winter MUFs and LUFs as a function of local time (from USAF Air Weather Service Pamphlet 105-36, February, 1975).

3.3.1 The Sudden Ionospheric Disturbance

The immediate effect of the arriving flare-related x-rays on the sunlit D-region is known as the *sudden ionospheric disturbance* (SID). Due to the popularity of HF radio frequencies (3–30 MHz), SIDs were first noticed at these frequencies and are often called *short wave fades* (SWF) for that reason. As the term implies, onset is usually sudden, and recovery is slow, much like the x-ray flux trace for the associated flare. The effect and duration decreases with increasing solar zenith angle.

A related term is the *sudden cosmic noise absorption*, or SCNA. This deals specifically with D-region absorption of radio waves originating from extraterrestrial sources, rather than absorption of man-made transmissions. The preferred measurement technique is *riometry*, to be addressed in Chapter 4.

3.3.2 Auroral Zone Absorption

Although visual aurora are spectacular, most of the kinetic energy from high energy precipitating particles is dissipated in the process of ionizing gas molecules in the lower ionosphere. Radio absorption as a result of auroral activity, *auroral zone absorption* (AZA), may last several hours, but individual peaks usually last only a few minutes. These short variations can produce marked localized absorption events (on rare occasions up to ~10 dB at 30 MHz) and usually indicate a bright arc or auroral substorm event within the auroral zone or polar cap. For a given auroral zone station, these large AZA 'spikes' are

most prominent near midnight (local geomagnetic time) and noon. However, on average, the maximum absorption occurs during late morning hours between 0800 and 1000 local geomagnetic time. During early morning and early evening, AZA is normally much less pronounced. On average, AZA at 30 MHz is <1 dB. Since auroral intensity and location are a function of local time and level of geomagnetic activity, AZA effects expand southward and intensify during geomagnetic storms (Hultqvist, 1969; Hargreaves, 1979).

3.4 Solar Proton Events and Polar Cap Absorption

3.4.1 Brief History

Of all solar flare effects, PCA events are generally longest in duration, sometimes lasting up to 10 days. Since the PCA phenomenon is actually a frequency-specific effect caused by solar protons, some purists prefer the term *solar proton event* (SPE). However, since this study deals specifically with HF and lower VHF absorption, we will continue to use the term PCA.

Bailey (1957, 1959) is believed to have been the first to describe and correctly postulate a cause for PCAs after his study of VHF absorption in the auroral zone and polar cap after a solar flare in February, 1956. Prior to Bailey's work, polar *blackouts* were considered merely special cases of auroral absorption, somehow associated with particles of such high energy that they could penetrate

the atmosphere to ground level; *i.e.*, a *ground level event* (GLE).

Subsequently, Hakura *et al.* (1958) described two cases, one each in 1957 and 1958, in which the absorption event began *before* the sudden commencement geomagnetic disturbance, yet neither case involved a GLE. Therefore, Bailey, along with Reid and Collins (1959), concluded that flares could produce particles of sufficient kinetic energy to penetrate to D-region heights resulting in enhanced absorption, but of insufficient energy to penetrate to ground level; the lower end of the particle energy spectrum responsible for PCA effects was calculated to be ~ 10 MeV (Bailey, 1964; Reid, 1967).

The next logical course of action was to make direct observations of these particles. Since ionospheric effects were concentrated in polar regions, a consequence of geomagnetic field line geometry discussed earlier, most attempts to make direct particle measurements were conducted at high latitudes.

The three platforms capable of approaching D-region heights were balloons, rockets, and orbiting satellites. Each had advantages, as well as certain drawbacks. Balloons were capable of *in situ* measurement for a short period of time but were generally limited to the lowest 30–35 km below nominal D-region heights; only very high energy particles (>80 – 100 MeV) penetrate to this level and below. Rockets could reach higher altitudes, thereby detecting lower energy particles (<1 MeV), but time of flight was relatively short. The advent of orbiting satellites brought the capability of detecting particles down to keV energies, enhancing the level of knowledge about the earth's plasmasphere and magnetosphere, but were unable to directly measure within the D-region. Nonetheless,

the combination of these methods supplied a wealth of knowledge regarding the nature of energetic particles of solar origin.

The Concept of Particle Storage

One question tackled by the pioneers in PCA research was the slow decay of PCA events which in some cases lasted several days. Assuming these MeV particles were flare-related, supposedly ejected in a relatively short burst, why would the absorption effects last so long? Wouldn't the cloud of protons simply sweep by earth and go on past 1 AU as quickly as they came? Several theories have been proposed to explain this (*e.g.* Gold, 1959; Parker, 1959; and many others), but most now agree that some sort of storage or delay process takes place as a result of irregularities within the post-flare IMF. A thorough discussion of these theories is unnecessary here; the important concept is that some storage process within the solar wind is responsible for the slow decay time of a PCA event.

Penetration Depth and Cutoff Latitude of Solar Protons

Störmer (1955) developed the theory of motion of charged particles in a dipole magnetic field that at a given geomagnetic latitude, there is some cutoff rigidity, given by $R_c = 14.9 \cos^4 \Phi$, where Φ is the geomagnetic latitude and R_c is in gigavolts (10^9 volts). Particles with rigidity lower than this value are forbidden entry at latitudes lower than Φ . Thus, by knowing particle energy, we can determine a cutoff latitude below which the particle will not be expected

to reach the atmosphere. This relationship was developed for a simple dipole magnetic field.

From observations taken during the late 1950s and early 1960s, it became apparent that actual cutoff rigidities were much lower. One reason is that the earth is not a strict dipole. Furthermore, during geomagnetically disturbed periods, cutoff latitudes decrease as the auroral oval expands equatorward, effectively enlarging the polar region enclosed within it. For example, Freier *et al.* (1959) detected protons with energies well below theoretical cutoff energies during a geomagnetic storm, and Reid and Leinbach (1961) noticed an equatorward displacement of PCA effects after the onset of a geomagnetic storm.

Reid and Sauer (1967) adapted the dipole model to a more realistic model. The two models are compared in Fig 3.7, which shows cutoff latitude as a function of proton energy valid near geomagnetic local midnight. Bailey (1959) (among others) took the Störmer cutoff function and developed an expression for the height to which a particle with given energy could penetrate at a given geomagnetic latitude. A graphical representation is shown at Fig 3.8. This was completed prior to subsequent studies which uncovered a diurnal variation of cutoff rigidity and thus cutoff latitude.

Diurnal Variation of Cutoff Latitude

Stone (1964) and Reid and Sauer (1967a) found a local time dependence of geomagnetic cutoff; nighttime cutoff latitudes were lower than daytime. This seems to be related to the equatorward displacement of the auroral oval, which

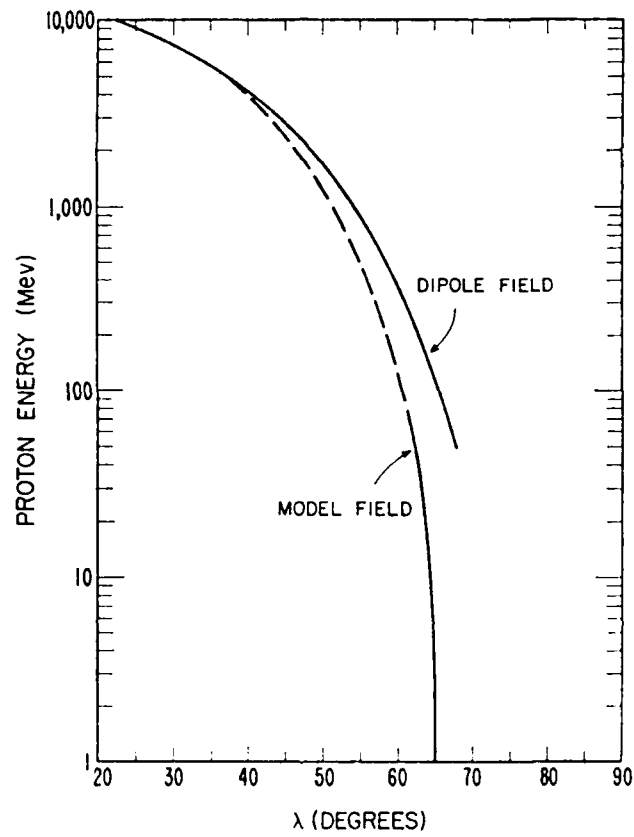


Figure 3.7: Model vs. Störmer Geomagnetic Cutoffs. Both are valid near geomagnetic local midnight (from Reid and Sauer, 1967).

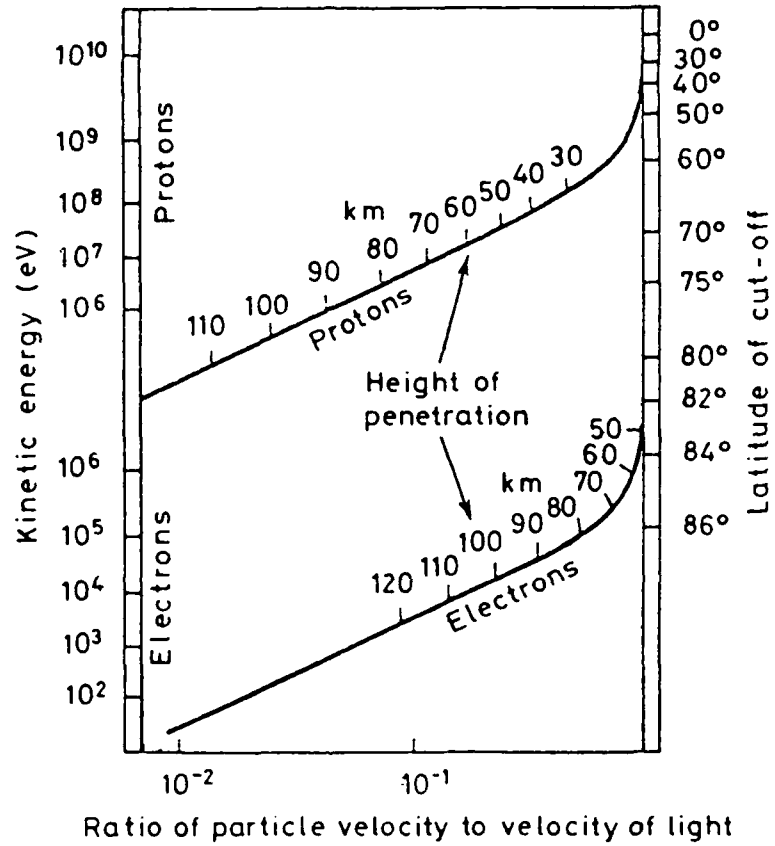


Figure 3.8: Penetration of protons and electrons, and cutoff latitudes as functions of velocity (from Hargreaves, 1979, after Bailey, 1959).

has the same diurnal character, and explains the *midday recovery*, a marked decrease in absorption noted around local noon, especially near the equatorward boundary of the affected polar region. Reid and Sauer associated this to a local change in *pitch angle*; *i.e.*, the angle between a particle's velocity vector and the local magnetic field vector. Thus, the pitch angle is related directly to particle rigidity and inversely to local magnetic field strength.

As will be shown later, this diurnal cutoff variation has possible implications with respect to delayed ionospheric response to particle flux variations detected at geosynchronous altitudes.

North-South Asymmetry of Particle Access

Evans and Stone (1969) described an event where solar protons were observed to arrive at the south polar cap within an hour of the observed flare, yet protons of the same energy were not observed at the north polar cap until some 20 hours later. They attempted to use this as evidence for a closed magnetosphere, suggesting that particles must enter the magnetosphere by slow diffusion via the magnetotail.

Van Allen *et al.* (1971) disputed this explanation, asserting that the open model allows for delayed access at one pole assuming that energetic particle flow within the near-earth IMF is anisotropic. Fig 3.9 illustrates an open model and anisotropy vectors showing how relative orientations of the geomagnetic field and IMF could conceivably shield one pole from the brunt of the corpuscular onslaught. Generally, these marked delays are exceptions, yet the geometry pro-

posed in the latter article may explain differences in PCA magnitude between magnetic *conjugates* points on earth which lie at opposite ends of a particular closed field line.

3.4.2 Ionospheric Effects

As cosmic ray physicists were busy figuring out how energetic particles made their way into the upper atmosphere, ionospheric and upper atmospheric specialists attempted to explain the ionization and resultant effects upon radio propagation.

Ionization

The ionization process during proton events is simpler chemically than during quiet times. Incoming energetic protons, penetrating deep into the polar ionosphere (depending on their kinetic energies) are capable of ionizing any atmospheric constituent (N_2 , O_2 , Ar , N , O , etc.), principally O_2 (90%) (Zmuda and Potemra, 1972), dramatically increasing electron densities, and lowering the D-region, sometimes down to 35 km. Mitra (1974) and Chamberlain and Hunten (1987) give comprehensive descriptions of ionospheric chemical effects due to solar flares and their ejecta; these details are not discussed here.

PCA event morphology

Using ionosonde data from 50 stations in the northern polar region, Hakkura (1967) completed detailed studies of several PCA events. Based on the

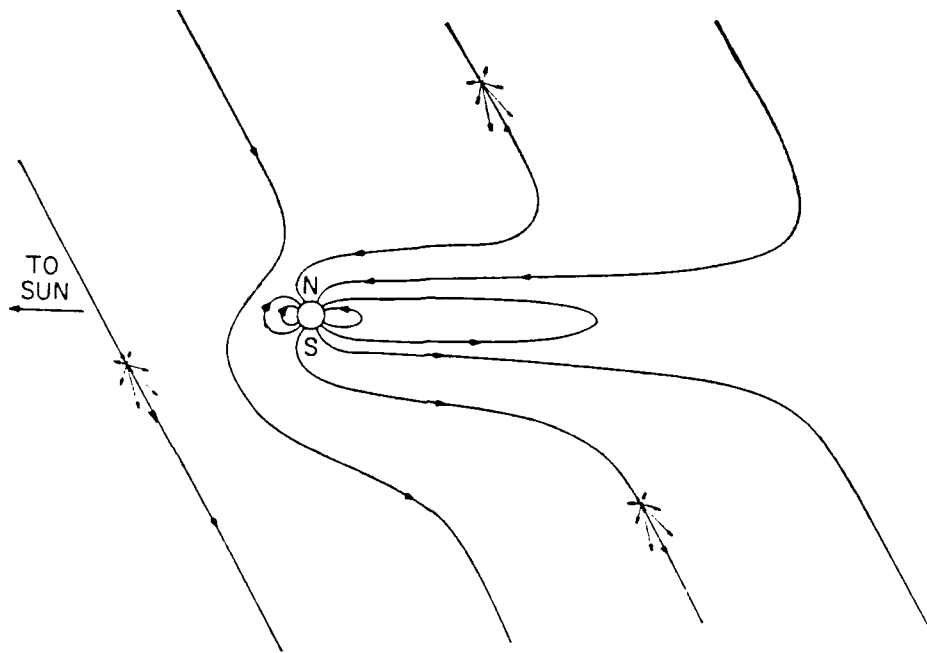


Figure 3.9: IMF-Magnetosphere connection model (from Van Allen *et al.*, 1971).

behavior he observed, he divided the initial phase of a PCA into three stages.

Stage 1 was confined to a quite small area above 80° corrected geomagnetic latitude (CGL) on the dayside, possibly corresponding to the polar cusp. Using low-orbiting satellite data, he found that the major ionizing agents during Stage 1 were high energy electrons. Within an hour or so later, Stage 2 begins, characterized by a 'sudden and outstanding' intensification within the polar cap down to about 65° CGL. The major ionizing agents in Stage 2 were protons. Stage 3 was the more gradual (several hours) increase of ionization across the polar cap to complete the total 'blackout' down to $\sim 60^\circ$ CGL. Protons and α -particles were the principal ionizing agents. In three-fourths of the cases he studied, proton and α -particle fluxes were nearly equal during this stage. In those cases, the threshold rigidity for producing PCA effects was greater for α -particles than for protons. Hakura concluded, therefore, that α -particles define the lower latitude limit of PCA effects, since higher rigidity energetic particles imply lower cutoff latitudes.

From these results, at a given group of stations, we might expect to see an equatorward progression during the initial phase. The main phase or 'plateau' of the event, when proton fluxes level off, is generally believed to be characterized by rather uniform absorption, with two exceptions. Near the auroral zones, where cutoffs show diurnal variations, there is a marked *midday recovery* where absorption decreases for 3-4 hours (Leinbach, 1967). The other exception is that stations which experience both a day and night (at ionospheric heights) will notice that daytime absorption is 4-5 times nighttime absorption, due to the daytime photoionization contributed by solar UV, x-rays, and Lyman- α . Gillmor (1963)

studied this effect by comparing an Antarctic station and its magnetic conjugate. The northern station was continuously sunlit, while the Antarctic station experienced both a day and a night at D-region heights. He found that the ratio of daytime to nighttime absorption at 30 MHz was ~ 5.3 (see Fig 3.10).

More recently, Armstrong *et al.* (1989) studied the relationship between certain particle energies and resultant absorption during PCA events occurring from 1982 to 1985 at South Pole Station. For events of >0.1 dB, they found that solar and interplanetary protons of <10 MeV were the dominant contributors at 30 MHz, specifically those in the 2–4 MeV range. This is consistent with Fig 3.8, which shows a cutoff latitude for 2–4 MeV protons near $73\text{--}75^\circ$, the approximate geomagnetic latitude at South Pole Station. In their study, the contribution of α -particles was found to be quite small as a percentage of the total absorption, with rare exceptions ($\sim 10\%$ at the peak of a 1983 event).

This study is not specifically concerned with relating absorption at a specific frequency to specific proton energies or to asymmetry between north and south polar effects. We are, however, interested in looking a little more closely at Hakura's result showing an equatorward expansion of PCA effects during the onset. With this general aim established, we now move on to describe our data sources and an actual PCA event case study.

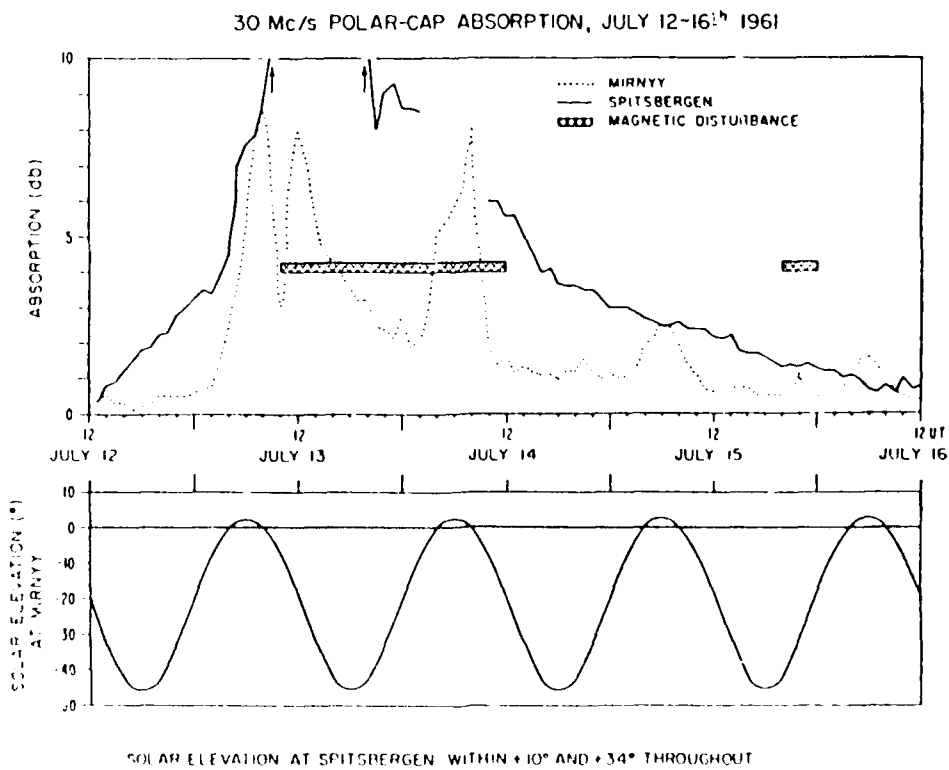


Figure 3.10: Comparison of absorption at 30 MHz (Mc/s) for magnetic conjugates. During daylight hours at Mirny (solar elevation $> 0^\circ$), absorption is essentially equal to the Spitsbergen value. Otherwise, values are much lower than at the continuously daylit station (from Gillmor, 1963).

Chapter 4

Instrumentation and Data

Sources

4.1 Satellite-Borne Sensors

Both x-ray and particle data used for reference in this study are from measurements by GOES-7 (Geostationary Operational Environment Satellite). Except on extremely rare occasions, the orbit of GOES-7 is entirely within earth's magnetosphere, the only exceptions being at local noon during extreme magnetospheric compression from an abnormally fast and/or dense solar wind. At the time of the event we will study, GOES-7 was positioned over the equator at $\sim 100^\circ\text{W}$ longitude.

Particle sensors aboard GOES-7 are capable of measuring electron fluxes with energies of >2 MeV and proton fluxes in several channels between 0.8 and

400 MeV, with an additional sensor capable of detecting fluxes >370 MeV. GOES-7 is also equipped with a radiometer capable of measuring x-ray flux in two channels: $1-8\text{\AA}$ (soft x-rays) and $0.5-3.0\text{\AA}$ (hard x-rays) (NASA, 1982).

X-ray flux is one means of classifying solar flares. Each flare is classified by its peak flux in the $1-8\text{\AA}$ range. These classes are as follows: *X* for $> 10^{-4}\text{Wm}^{-2}$, *M* for $1-9.9 \times 10^{-5}\text{Wm}^{-2}$, and *C* for $1-9.9 \times 10^{-6}\text{Wm}^{-2}$. For example, a flare with peak x-ray flux of $3.4 \times 10^{-4}\text{Wm}^{-2}$ would be classified X3.4. Generally, only M- or X-class flares have significant ionospheric consequences with regard to absorption.

4.2 Ground-Based Sensors

Amundsen-Scott South Pole Station, Antarctica is located at the geographic south pole, defined by axis of rotation (see Fig 4.1). For geomagnetic studies it is common to define a particular location according to its *L-parameter*, where *L* is the distance from earth's center to the equatorial crossing of the field line passing through the location in question (McIlwain, 1961). At South Pole Station, $L \simeq 13.2$, so that a field line emanating from the earth at the site would be at $\sim 13.2 R_e$ over the equator of a dipole field. Although earth's field is not strictly dipole, along most geomagnetic field lines *L* is constant to within 1% (Hargreaves, 1979). Another common representation is the *invariant latitude* Φ , defined as

$$\Phi = \sqrt{\cos^{-1}\left(\frac{1}{L}\right)} \quad (4.1)$$

For South Pole Station, then, $\Phi \simeq 74$. Refer to Fig 4.2 to see the orientation of invariant latitudes near South Pole Station. The following instruments, located at South Pole Station, are relevant to this study.

4.2.1 Magnetometer

A magnetometer is a device used to measure magnetic field strength at a given location. The system in operation at South Pole Station measures the north-south component (H), the east-west component (D), and the local vertical component (Z) of the magnetic field vector, \vec{B} . The preferred unit of measurement is the nanotesla ($\text{nT} = 10^{-9} \text{Wb m}^{-2}$). We will look at all three component sensors, primarily the H -sensor to locate geomagnetically quiet periods, since we want to minimize absorption effects of auroral substorms and other localized transitory effects.

4.2.2 Riometers

Mitra and Shain (1954) first proposed measuring atmospheric absorption of radio waves of extraterrestrial origin. Little and Leinbach (1958, 1959) adapted this principle to the *riometer* (relative ionospheric opacity meter) for studies specifically suited to the polar and auroral ionosphere, where PCA and AZA are important. Using riometry, absorption can be calculated for specific frequencies even under total 'blackout' conditions. Previously, scientists had attempted to measure absorption events by simply monitoring station-to-station radio transmissions, a technique rendered virtually useless when the signal was totally ab-

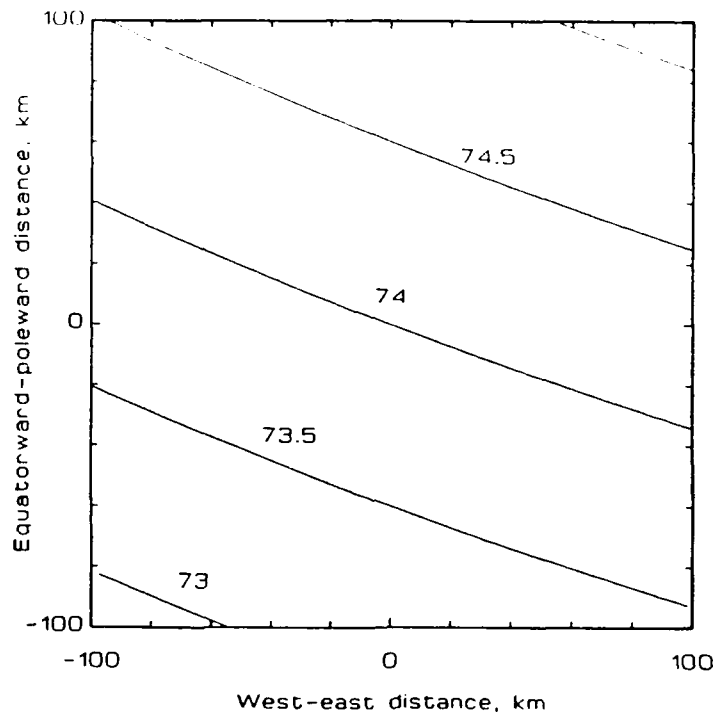


Figure 4.2: Invariant latitudes near South Pole Station. This is also how the South Pole IRIS is oriented.

sorbed in the D-region.

Basis of Operation

Our galaxy is made up of hot gases and stars, each emitting electromagnetic radiation. A minute fraction of this radiation is received at earth, where it can either be transmitted through the atmosphere, absorbed, or reflected, depending on the extinction properties of the intervening medium, namely, the atmosphere and ionosphere. By continual monitoring with a vertically pointed antenna, the riometer converts the downwelling radiation at a specific frequency into a measurable current or voltage signal.

A broadbeam riometer typically operates with a half-power (-3 dB) beam width of 60° , corresponding to a circular projection on the ionosphere (~ 90 km altitude) of approximately 90 km in diameter (Detrick and Rosenberg, 1990). The University of Maryland has operated such a system at South Pole Station since 1982, monitoring four frequencies: 20.5, 30, 38.2, and 51.4 MHz.

To determine absorption using this method, recorded voltages values must be compared to a baseline or reference value.

Quiet Day Curve

The *quiet day curve* (QDC) is a baseline time series for a given site and time of year. Numerous methods have been employed to calculate the QDC. The University of Maryland employs an inflection point method developed by Krishnaswamy, *et al.* (1985). This method involves making a frequency distribution

of voltage values vs. frequency of occurrence during corresponding time bins for each day in a month of collected data. The voltage value corresponding to the upper inflection point of the frequency distribution becomes the QDC value for that time bin. For example, suppose we want our bin to be 10 minutes in length. Since there are 1440 minutes in a day, there will be 144 frequency distributions for each monthly QDC computation. This method is employed for the broadband riometer, as well as for *each beam* of the IRIS array, which uses a 2-minute bin (Detrick, 1990).

Calculation of Absorption

Using raw data and the QDC, absorption is calculated using the definition of the decibel:

$$Abs(dB) = 10 \log\left(\frac{V_0}{V}\right) \quad (4.2)$$

where V is the observed voltage and V_0 is the QDC voltage value. For a broadband riometer of this type, the absorption per unit vertical column can be approximated as 80% of the calculated broadband value (Armstrong *et al.*, 1989). Note that absorption is expressed as a positive value. Negative absorption values (when $V > V_0$) normally indicate noise, natural or man-made in origin, which can temporarily result in enhanced voltage readings relative to the QDC value, thus causing an anomalous short-term reduction in the calculated absorption value.

4.2.3 The University of Maryland Imaging Riometer for Ionospheric Studies (IRIS)

Obviously, a broadbeam riometer has a strict limitation; namely, there is a wide field-of-view (FOV) which can only be represented by one value at a given time. Transient ionospheric phenomena such as auroral arcs or traveling surges may move into and out of the field of view within a few minutes; smaller-scale structures may form and dissipate within a few tens of seconds. In response to the natural desire to study this fine structure, the upper atmospheric research group of University of Maryland's Institute for Physical Science and Technology (IPST) developed the Imaging Riometer for Ionospheric Studies (IRIS). Installation at South Pole Station was completed in January, 1988.

IRIS operates at 38.2 MHz and monitors a 7×7 array of 49 independent beams, covering an ionospheric area (at ~ 90 km altitude) of approximately 200 km square. The sampling rate for each beam is 1 second (Detrick and Rosenberg, 1990).

Display of IRIS Data

Fig 4.3 shows the ionospheric projection of both the broadbeam riometer and IRIS. A sampling of computed IRIS quiet day curves is included in Fig 4.4. As you look at the displayed array, you are essentially looking 'up' at the radio sky with geomagnetic south at the top; east is toward the right. The actual orientation is the same as shown back in Fig 4.2 so that geomagnetic south is

toward the upper right rotated $\sim 20^\circ$ from the vertical axis. Note that in Fig 4.4 the center beam QDC is a constant throughout the day since it is looking at zenith, thus parallel to earth's rotation axis. Also, notice the procession of various peaks around the array due to rotation. The highest peak corresponds to radiation emitted by the center of our galaxy.

In addition to simply displaying each beam's time series, Detrick and Rosenberg (1990) developed software to 'image' absorption data, allowing 'visual' inspection of the radio sky at 38.2 MHz. Orientation of the image is the same as discussed in the previous paragraph. There are several options to choose from when plotting IRIS images. Two of these deal with scaling. The first option calculates absorption values using the QDC as the zero level, as discussed above. Another alternative lets us subtract off the minimum absorption value for each beam during the time period being plotted, thus allowing us to highlight changes relative to the background absorption.

Options for plot resolution are 10 seconds, 1 minute, and 10 minutes. With 10-second resolution, the routine plots the data for each beam for the first second of the 10-second interval. For 1-minute and 10-minute resolution, the peak value for each beam during that interval is plotted. We will plot using 1-minute resolution.

Prior to plotting, the imaging program subjects IRIS data to an exponential smoother.

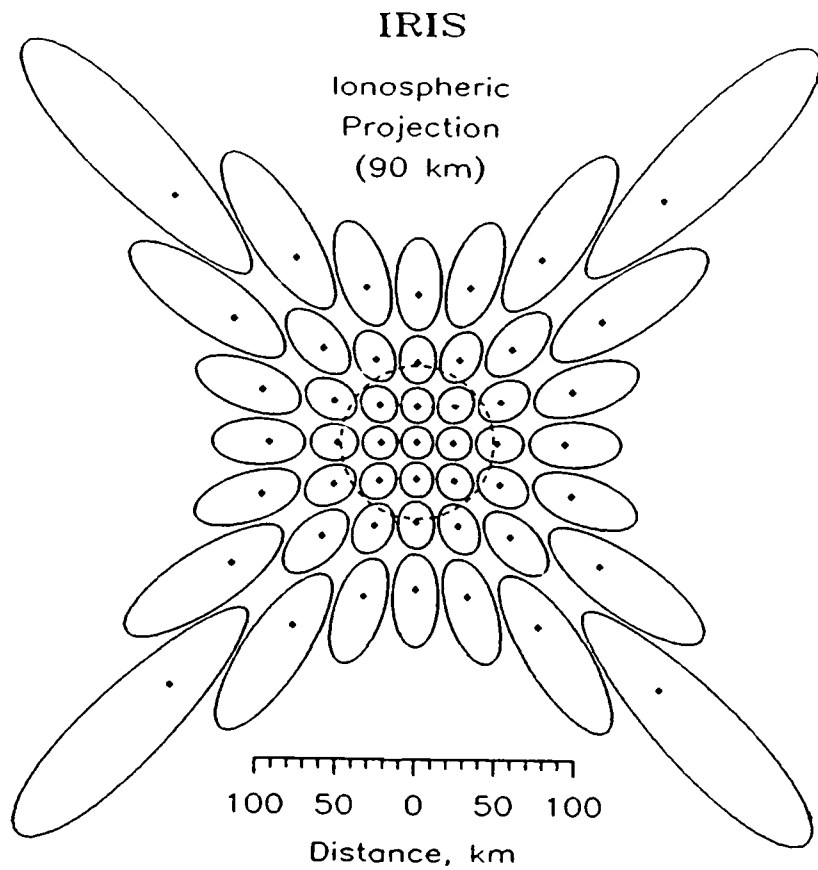
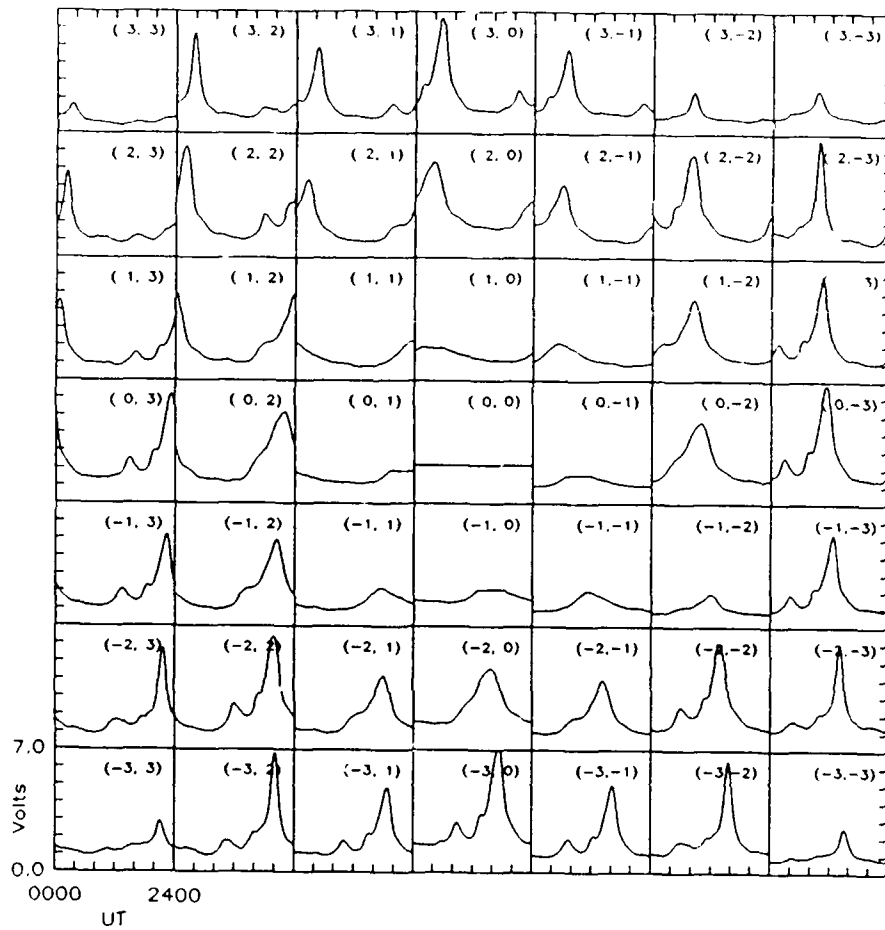


Figure 4.3: Ionospheric projection of IRIS beams (from Detrick and Rosenberg, 1990).



South Pole IRIS, 19 October, 1989

Figure 4.4: IRIS Quiet Day Curves for October 1989.

Previous Studies Using IRIS

Primarily, IRIS was developed to study the short-lived small-scale absorption features associated with auroral activity. In fact, the effort has been to 'weed out' PCA days in order to study only short-term auroral absorption effects. IRIS also provides the opportunity to image the radio sky on the dayside. Previously, the only images available were nighttime photographs using an all-sky camera. Although no papers dealing with actual event analysis using IRIS have been published, the group headed by T. J. Rosenberg has given several talks on the system, its capabilities, and analysis of daytime and nighttime small-scale absorption features within IRIS's FOV.

Chapter 5

Examination of a PCA Event

Using IRIS

5.1 The Game Plan

This is the first attempt to deal specifically with a PCA event using IRIS data. We wish to investigate the tendency or lack of tendency for movement of features embedded within the PCA across the array. In other words, the questions we wish to pursue are as follows:

- Do characteristic features in the time series lag or lead the same features in a beam elsewhere in the array?
- Earlier, we discussed the tendency for a PCA to begin near the pole and spread southward, eventually filling in the auroral oval. Can we detect an equatorward progression during the onset phase?

- Using imaged data, do we notice a progression of effects within the array, either during onset or the early main phase of the PCA event?

5.1.1 Filtering the Data

In an earlier section we stated that previous IRIS studies involved elimination of PCA days in order to study only auroral, short-term events. By definition, this study will have the exact opposite aim: we wish to filter out the short time scale components in order to study a PCA event. The best way to ensure minimum contamination by auroral or substorm-related absorption is to make sure we only study time segments within an event when the local geomagnetic field is relatively quiet. Luckily, South Pole magnetometer data are available for this determination.

The next step involves mathematical filtering of the data. In this study, we use the filtering scheme described by Duchon (1979), which uses weights calculated by

$$w(k) = \sigma \left[\frac{\sin(2\pi f_{c2} k)}{\pi k} - \frac{\sin(2\pi f_{c1} k)}{\pi k} \right] \quad (5.1)$$

$$\sigma = \frac{\sin(\frac{\pi k}{n})}{\frac{\pi k}{n}} \quad (5.2)$$

where $w(k)$ is the weighting function at k discrete points, f_{c1} is the cut-in frequency (cycles per data time interval), f_{c2} is the cut-out frequency (cycles per data time interval), n is the number of weighting points on either side of the center weight, and σ is the Lanczos sigma factor. To get meaningful results, we

must be careful to choose n such that

$$n \geq \frac{1.3}{f_{c_2} - f_{c_1}} \quad (5.3)$$

The larger we can make n , the more well-defined the frequency response will be at the cut-in and cut-out frequency. For example, see the frequency response graphs in Fig 5.1 for a comparison between a low-pass situation ($f_{c_1} = 0$, $f_{c_2} = 0.1$) when $n = 13$ (the minimum value), $n = 30$, and $n = 40$. On the other hand, we must be careful not to choose n too large because we will lose the time interval $n\Delta t$ from each end of the time period to be filtered. For this study, we have chosen to set n to 2 times its minimum value, rounded to the nearest 5.

5.1.2 Beam Cross-Correlation

Using filtered data we will perform a cross-correlation between beams in the IRIS array. The strategy will be to perform a cross-correlation between the center beam and the other beams in the array.

In this case, we wish to investigate the possibility of both positive and negative lags; therefore, each lag correlation coefficient, r_L is given by

$$r_L = \frac{\bar{X}_t \bar{Y}_{t+L} - \bar{X} \bar{Y}}{s_x s_y} \quad (5.4)$$

where X_t and Y_t are the two compared time series, \bar{X} and \bar{Y} represent means of the respective series, L is the lag, and s_x and s_y are standard deviations of the respective series. If we consider N filtered observations, there will be $N - L$ terms in each cross-correlation calculation (Panofsky and Brier, 1958).

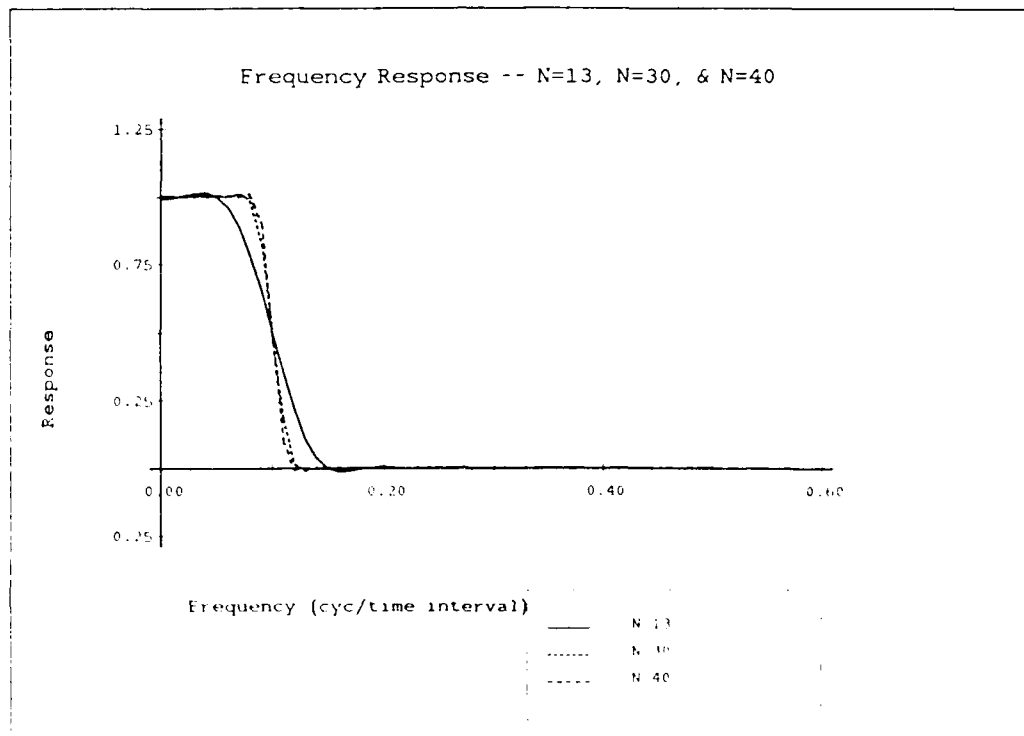


Figure 5.1: Frequency response function of a low-pass filter for $n = 13$, $n = 30$, and $n = 40$, $\Delta t = 1$ min, $f_{c_1} = 0$, $f_{c_2} = 0.1$, such that oscillations with periods less than 10 minutes ($\Delta t / (f_{c_2} - f_{c_1})$) will be filtered out.

Each calculation will yield a set of lag correlation values. We will then determine the lag corresponding to the maximum correlation value for each beam. (By basing these cross-correlations on the center beam (0,0), we know that maximum correlation of this beam with itself will always be at lag zero.) If we notice any patterns of leads or lags, we will examine the correlograms and look at the time series to see if we can notice lags or leads in any of the features (*i.e.* maxima and minima). With this information, we will attempt to offer a physical explanation of the results.

5.1.3 Visual Inspection of the Imaged Data

If we notice a significant result from the cross-correlation analysis, we will examine imaged data to see if we can verify feature delay patterns within the field of view.

5.1.4 Limitations and Assumptions

As in every study, there are certain assumptions and limitations we must state before proceeding further.

Quiet Day Curve Difficulties

Our first limitation is a direct result of logistics. Data tapes are routinely sent from South Pole station during southern hemisphere summer. Since we will consider data from October, 1989, the routine shipment of tapes covering that period have not yet arrived. The tapes in our possession, sent by special request,

cover only 11 days in October. Ideally, at least 2 weeks of data are required to compute a proper QDC. As a result, we are forced to use the QDC from December, 1988, normalized to the quietest of the 11 days in our possession. This may result in errors of up to $\sim .25$ dB.

Hardware Problems

Based on conversations with D.L. Detrick (1990), there seems to be a consistent problem with beams (3,-2) and (-1,-2) resulting in doubtful voltage values. Calculations involving these beams will be discarded. Additionally, a problem developed apparently developed on 19 October in beams (2,-1), (-3,2), and (-2,3). Voltage values go off-scale in these three beams after approximately 1300, 1540, and 1800 UT, respectively. Therefore, we will not consider calculations from these beams subsequent to their respective failure.

Assumptions

We shall assume that any fluctuations related to PCA are on time scales > 10 minutes, and that by filtering out the shorter period fluctuations we are merely eliminating instrument noise or quick magnetic field (*e.g.* Pi or Pc) pulsations. Unless stated otherwise below, fluctuations with periods < 10 minutes will be filtered out. We will use a time resolution of 10 seconds for all calculations.

5.2 The Solar Flare of 19 October 1989

At 1229 (all times UT) on 19 October 1989, the solar observatory at Ramey AFB, Puerto Rico reported the beginning of a solar flare in H α light. The H α event reached peak intensity at approximately 1300 and began a slow decline to pre-flare levels which lasted approximately 8 h. When the flare was first detected there was a simultaneous rapid rise in x-ray flux reported by the GOES-7 geosynchronous satellite. The peak soft x-ray flux was $1.3 \times 10^{-3} \text{ W m}^{-2}$ (classified X-13) at 1300. Following the maximum, x-ray flux dropped back to pre-flare levels at about 20/0100. The rapid rise and exponential decay shown in Fig 5.2 is typical of energetic flares.

5.2.1 Near-Earth Particle Environment

Within ~30 minutes from the detection of the flare, GOES-7 began to detect a sharp enhancement of energetic particle flux, which means it took the particles only ~38 minutes to travel from the sun to earth. In Fig 5.2, we see that during onset (~1300-1600) particles in the higher energy channels arrive before those in the lower energy channels, as expected. Fluxes in the highest energy channel began the main rise at ~1300 and began levelling off at ~1430. Particles in the lowest proton channel began rising toward the plateau just before 1400 and began levelling off at ~1600.

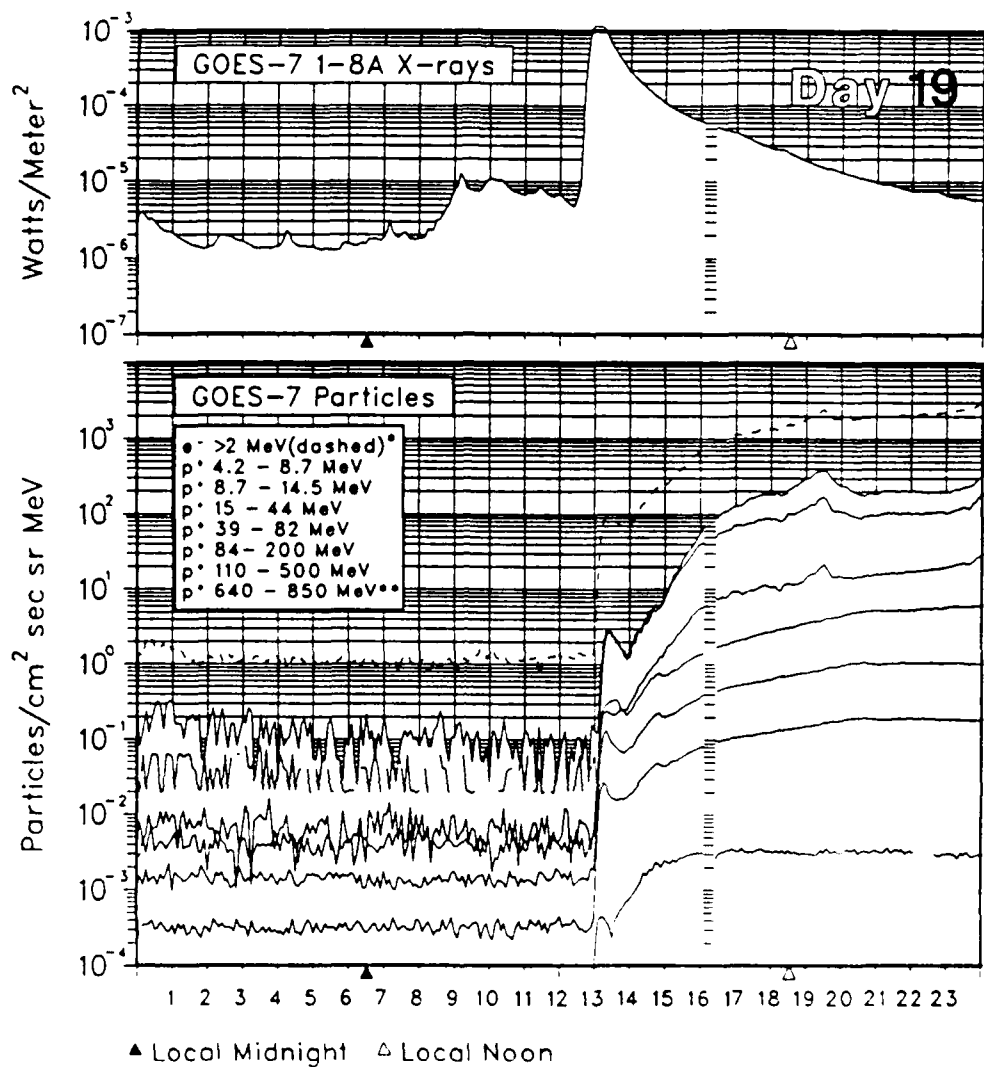


Figure 5.2: Near-earth soft x-ray and energetic particles recorded by GOES-7, 19 October 1989 (from *Solar Geophysical Data prompt reports*, NOAA, November, 1989, Part 1).

5.2.2 Examination of Magnetometer Data

After 1200 UT on 19 October, the local geomagnetic field was relatively quiet (Fig 5.3). This is fortunate because it suggests minimal contamination of our results from overhead auroral activity and AZA effects. Referring to Fig 5.3, we notice that traces in all three component sensors are particularly smooth during the period 1330–1630, after which rapid minor fluctuations set in; the latter coincide with similar fluctuations in GOES-7particle flux traces.

One interesting feature on the H- and Z-sensors is the impulse near 1300 UT. In response to enhanced EUV, UV, and x-ray fluxes associated with solar flares, conductivity in the ionosphere becomes enhanced, altering local electrical currents, and in turn, causing a kink in the H-sensor trace.

5.2.3 Examination of the IRIS Data

During the latter half of 19 October, there are a few features evident in the particle data shown in Fig 5.2, which we will examine closely. To see the ionospheric response to the solar flare and enhanced particle flux, refer to Fig 5.4, which is one column of filtered IRIS data for the latter half of 19 October.

Period 1 will cover the time from 1225 to 1250 corresponding to the initial D-region response to the x-ray flare (SCNA) prior to arrival of the flare-related energetic particles. The 1250 end-time corresponds to the beginning of anomalously low absorption values due to radio noise bursts associated with the solar flare.

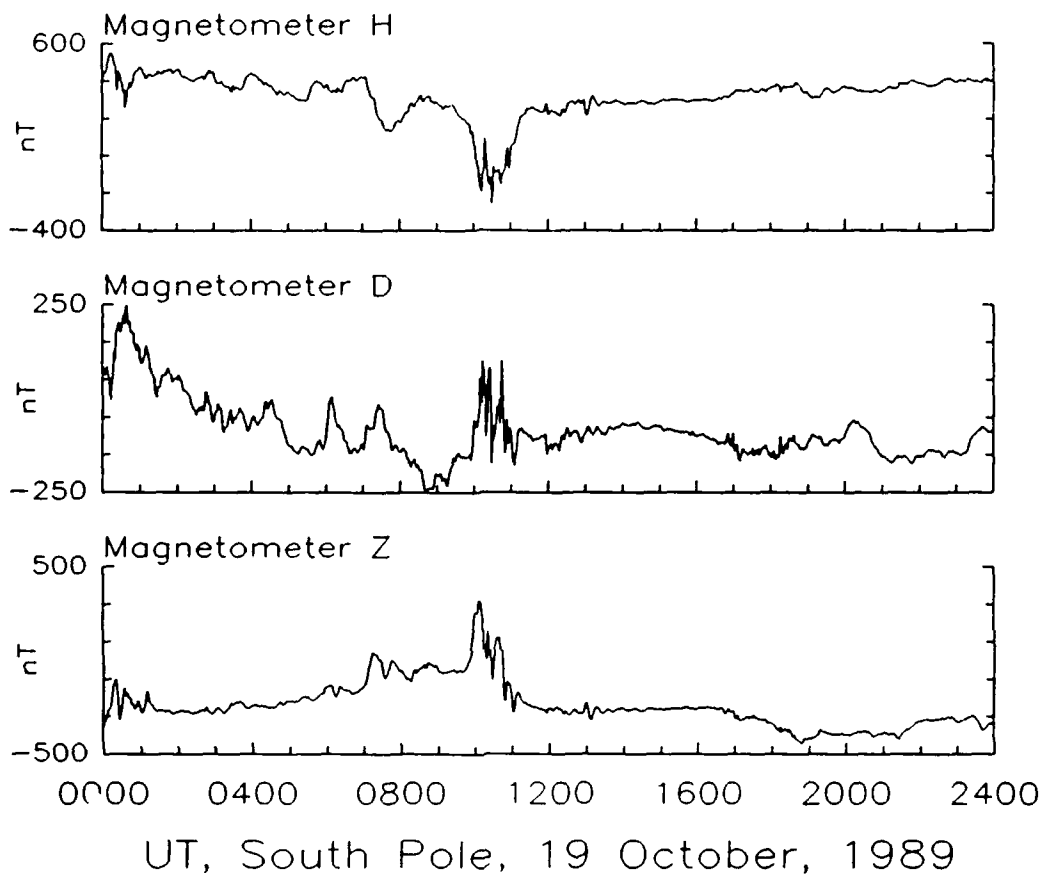


Figure 5.3: South Pole H-, D- and Z-sensor traces, 19 October 1989.

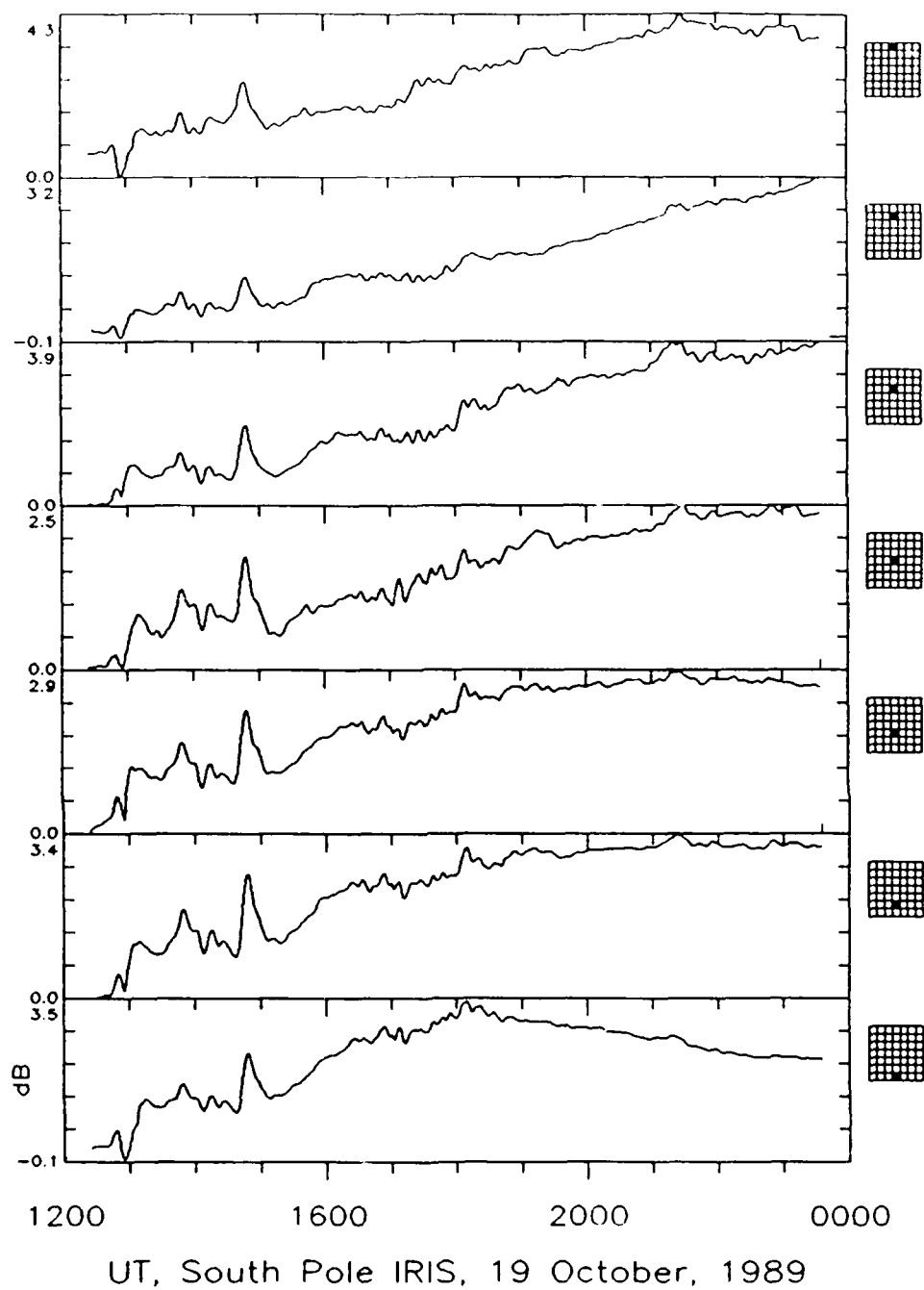


Figure 5.4: Filtered absorption plots in center column of the IRIS array for the period 1200-2400 UT, 19 October 1989.

Period 2 will cover the period 1300–1330, which corresponds to the initial jump in high energy particle flux from background levels to the first peak. There is still some noise storm contamination of this data.

Period 3, 1330–1600, covers the more gradual increase in particle flux to where fluxes appear to begin levelling off at the lowest energies.

Period 4 is a subset of Period 3 which covers the short interval, 1430–1500, corresponding to a small relative maximum or ‘bump’ evident on some of the particle channels at approximately 1445.

Finally, period 5 will cover 1630–2000, corresponding to a period of some fluctuations within the three lowest-energy proton channels.

5.2.4 Results of the Cross-Correlation Analysis

The results of cross-correlation between beam (0,0), the center beam, and all others in the array are displayed in Fig 5.5. Each of these figures is a display of the lag (in seconds) corresponding to the highest correlation, hereafter denoted $L_{r_{max}}$. Positive values are lags; negative values are leads; and a zero value indicates that the maximum correlation came at lag zero.

Period 1. 1225–1250, 19 October 1989

During the observed rise in x-ray flux, but prior to the arrival of flare-related energetic particles, we would expect nearly coincident response in all the beams. At this time of the year, approximately one month after the start of southern hemisphere spring, the D-region over the observing site is continuously

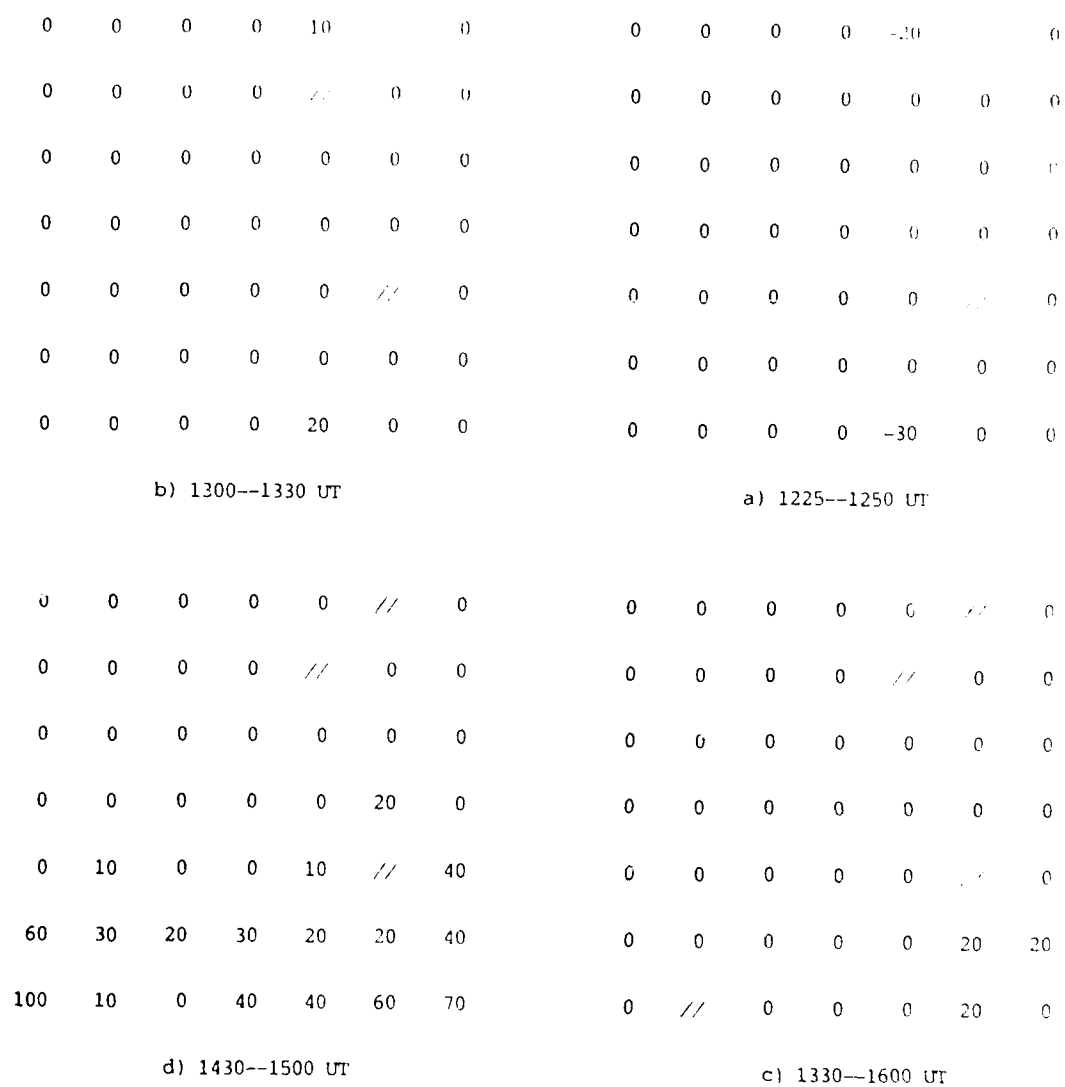


Figure 5.5: Lags corresponding to the maximum cross-correlation ($L_{r_{max}}$) with beam (0,0) for the following periods: a) 1225-1250 UT; b) 1300-1330 UT; c) 1330-1600 UT; and d) 1430-1500 UT, 19 October 1989. The period 1630-2000 UT is not shown because $L_{r_{max}} = 0$ for the entire array.

sunlit, therefore susceptible to the ionizing effects of x-rays. In Fig 5.5a we see this is the case. In all but two beams, $L_{r_{max}} = 0$. The two exceptions were lags of 20 and 30 second leads in beams (3,-1) and (-3,-1), respectively.

Figure 5.6 is a display of filtered absorption values for these beams and the center beam. Notice that radio burst spiking is markedly different in these beams and that in beams (3,-1) and (-3,-1) the response is wider and begins earlier than in beam (0,0) and prior to our 1250 endtime. This results in the leads calculated for these two beams. These are isolated instances and hardly significant.

Period 2, 1300–1330

As energetic particle flux first showed a sharp increase, absorption also showed a marked increase. In Fig 5.5b, we see that the highest correlation occurs at lag zero, with two exceptions. Beams (3,-1) and (-3,1) show lags for the same reason they showed leads during the 1225–1250 period. Since radio burst effects were more long-lived in these beams, the increase in absorption was delayed, showing up as lags (see Fig 5.6). Aside from these beams, the absorption increase from the initial sharp increase in solar protons was essentially simultaneous throughout the array.

Period 3, 1330–1600

This time frame covers the period during which energetic particle fluxes and absorption showed a long-term, more gradual rise toward their peak values for the day. This is the first case where there is any hint of a significant pattern

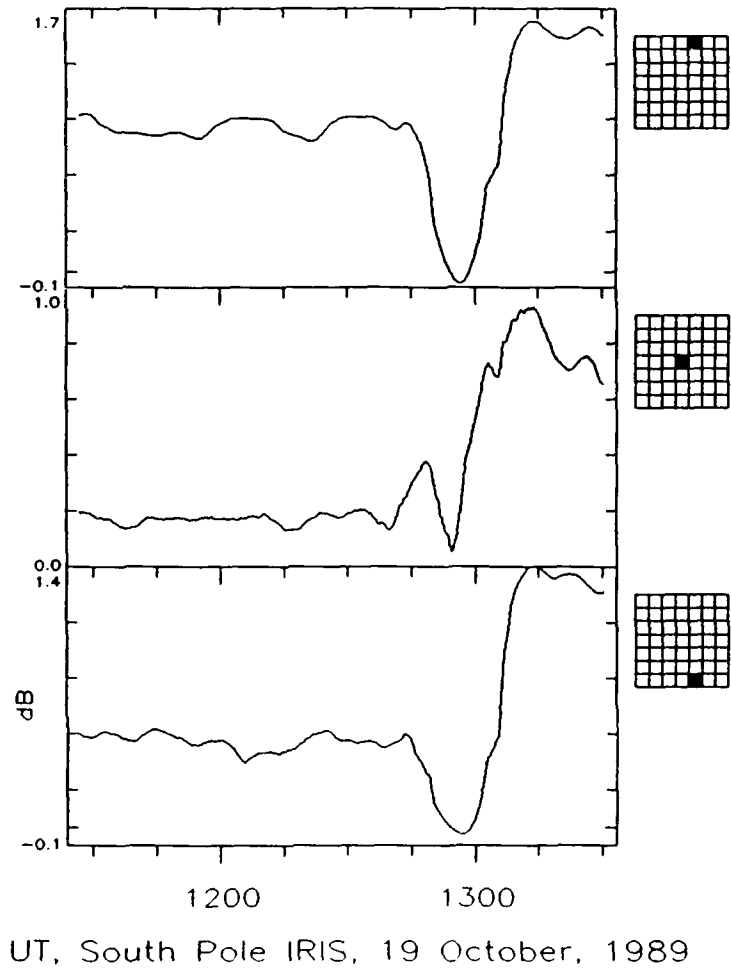


Figure 5.6: Filtered data plots of IRIS beams (3,-1), (0,0), and (-3,-1) including the period 1225–1250 UT (Period 1), 19 October 1989.

of time lags (Fig 5.5c). Note that generally, $L_{r_{max}} = 0$, but that there are three lags in the lower right (corresponding to the eastern/equatorward corner).

Since this was a rather long time period (150 minutes) we examined smaller chunks of time to see if we could find a period where the pattern was more pronounced and isolate a time interval which accounts for most of the lag correlation. In the process of doing this, we found that the only interesting activity coincides with the 'bump' contained in Period 4.

Period 4, 1430–1500

This period features a significant peak in absorption between 1445 and 1450, evidently echoing a nearly coincident bump in most of the GOES-7 particle channels. Fig 5.5d shows a striking pattern of lags clumped at the bottom (equatorward) portion of the array.

In an attempt to find the time frame with the maximum effect, we first found $L_{r_{max}}$ for successive 1-hour periods with start times stepped by 5 minutes. We see that the maximum effect occurred during the 1420–1520 time frame. Figure 5.7 shows the $L_{r_{max}}$ array for the periods beginning with 1415–1515, 1420–1520, and 1425–1525. With further refinement we narrowed this down even further to the 30-minutes between 1437 and 1507 (see Fig 5.8).

Correlograms which correspond to this time period are shown in Fig 5.9. Each correlogram is a graph of the lag correlation coefficient r_L for lags from $-L_{max}$ to $+L_{max}$, where L is the maximum lag. If the maximum r_L for any particular beam corresponds to a positive L , then time series features for that

0	0	0	0	0	//	0	30	30	0	-10	-30	//	0
0	0	0	0	//	0	20	0	0	20	0	//	0	50
0	0	0	0	0	0	0	0	30	0	20	40	0	20
0	0	0	0	0	20	0	40	40	20	0	30	70	40
0	0	0	0	0	//	30	30	50	30	40	40	//	90
140	50	20	20	20	30	40	200	100	70	60	70	80	90
300	50	0	50	50	110	110	300	80	40	90	90	150	150

1415—1515 UT

1420—1520 UT

0	0	0	0	-10	//	0
0	0	0	0	//	0	20
0	0	0	0	10	0	10
0	0	0	0	10	50	20
10	20	0	10	20	//	60
170	60	40	30	40	50	60
300	40	0	50	60	100	100

1425—1525 UT

Figure 5.7: Lags corresponding to the maximum cross-correlation ($L_{r_{max}}$) with beam (0,0) for the periods 1415–1515, 1420–1520, and 1425–1525 UT, 19 October 1989.

0	0	-10	-30	-40	//	-10
-10	0	20	0	//	0	40
0	20	0	20	40	0	30
20	20	20	0	40	70	50
30	40	30	40	50	//	80
140	90	60	60	70	70	90
210	80	40	90	90	130	130

1437--1507 UT

Figure 5.8: Lags corresponding to the maximum cross-correlation ($L_{r_{max}}$) with beam (0,0) for the period 1437-1507 UT, 19 October 1989.

beam lag behind those in the center beam. Conversely, if the peak corresponds to a negative value for L , then features within that beam lead those in the center beam. We see statistically that there is generally a delay in effects as we move from the top (poleward side) to the bottom (equatorward side) of the field of view. Let us now examine some actual data plots for this period.

Figure 5.10 shows the middle column of filtered IRIS absorption values for the period 1415–1515. Here we see the local peak in absorption at approximately 1447 with some beams apparently leading or lagging the central beam. Visually, it is difficult to determine the time lag or lead of a particular feature. By looking at actual values in the time series, we found the peak for each beam at the following times:

<u>Beam</u>	<u>T_{max}</u>	<u>Lag (sec)</u>
(3,0)	14:47:00	-20
(2,0)	14:47:20	± 00
(1,0)	14:47:40	+20
(0,0)	14:47:20	± 00
(-1,0)	14:47:30	+10
(-2,0)	14:47:50	+50
(-3,0)	14:47:50	+50

Figure 5.11 shows the array of lags using the above method for *this particular maximum* near 1447. The pattern is not precisely the same as in Fig 5.8, but

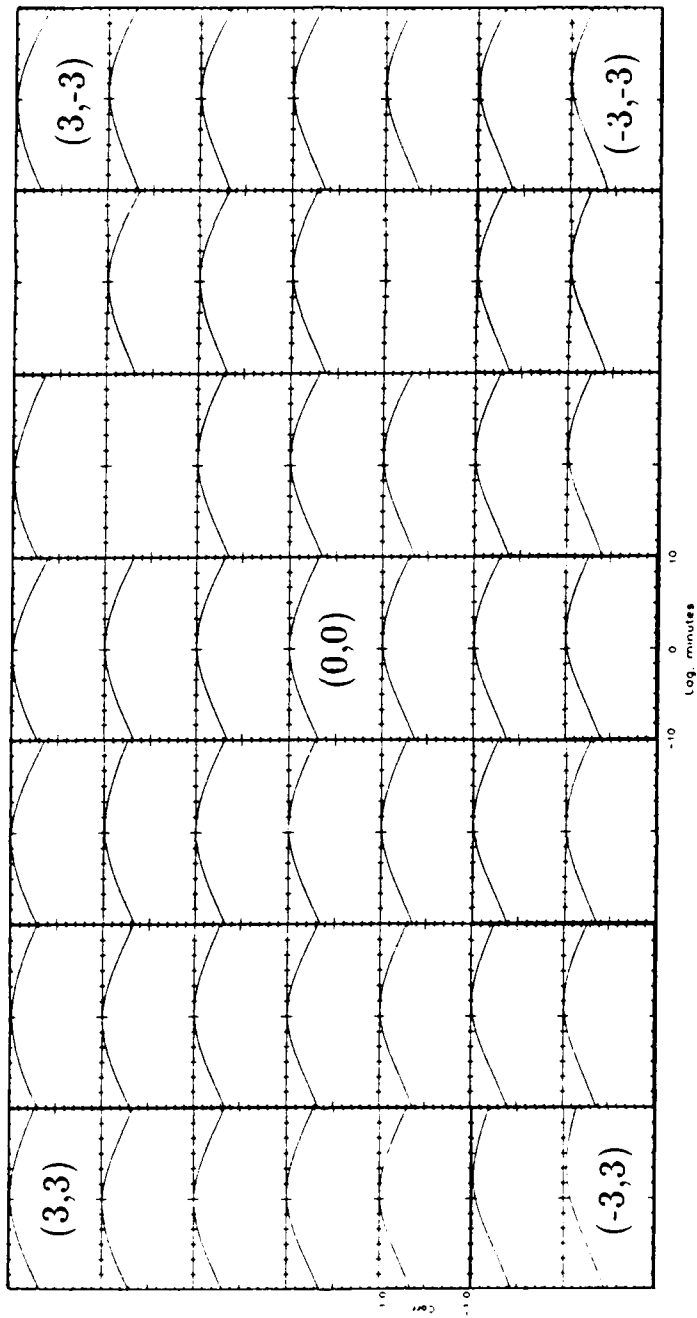
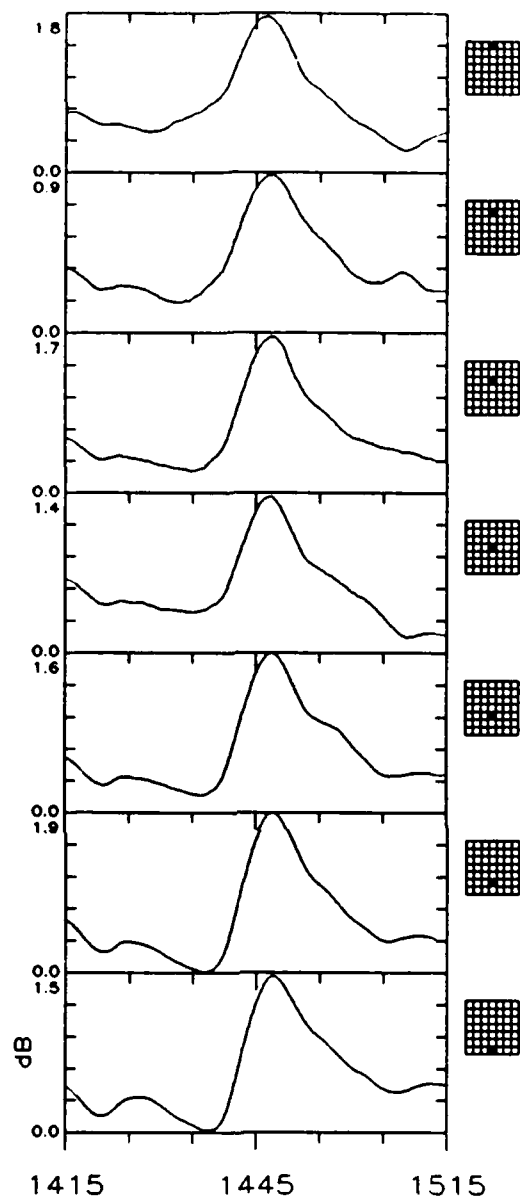


Figure 5.9: Collection of correlograms for the period 1437–1507 UT, 19 October 1989.



UT, South Pole IRIS, 19 October, 1989

Figure 5.10: Filtered IRIS data plots in the middle column for the period 1415–1515 UT, 19 October 1989.

generally, lags increase toward the bottom and right side of the array, while leads are limited to the top.

Period 5, 1630–2000

Period 5 is the more gradual rise toward the plateau of the event. We had expected this to be an interesting period due to the rapid pulses in particle flux recorded by GOES-7. However, when the cross-correlation was complete we were left with a null result; $L_{r_{max}} = 0$ for the entire array. The result persisted even when considering smaller time chunks.

5.2.5 Discussion of the Imaged Data

We found some evidence for delayed effects in certain parts of the array during Period 4, so let us now examine some of the imaged data for some ‘visual’ evidence. Remember, however, that data for these plots are unfiltered.

Since the main feature during Period 4 is a short-term enhancement superimposed upon the already rising particle flux, we will enable the option which subtracts from each beam the minimum absorption value during the period to be plotted. In Fig 5.12 we see that beginning just after 1430, an area of higher absorption values entered the field of view, eventually spreading downward (equatorward), intensifying, and reaching a peak between 1447 and 1449. After the peak, absorption begins to subside, first in the upper right of the image, then gradually down to the equatorward edge by ~ 1520 , with some patches of residual enhanced absorption left over.

-60	60	0	-20	-80	//	10
-50	10	20	0	//	0	60
-20	0	20	20	10	20	60
0	0	10	0	10	50	40
0	20	20	10	30	//	60
20	30	20	50	40	40	60
100	20	20	50	30	70	80

Figure 5.11: Lag in seconds relative to the center beam for the absorption peak occurring near 1447 UT, 19 October 1989.

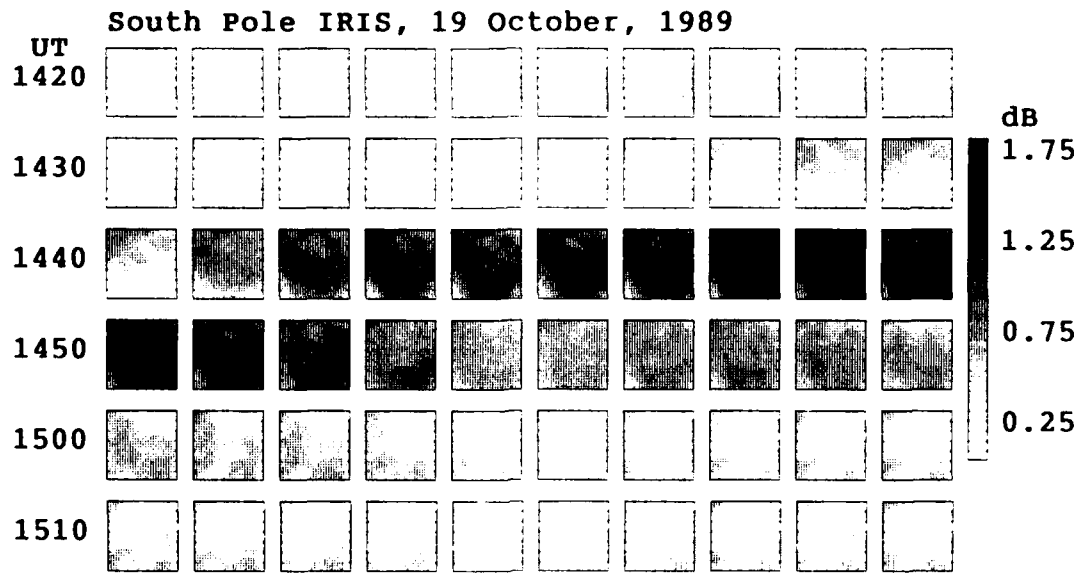


Figure 5.12: Imaged IRIS data for 19 October 1989, 1420–1520 UT.

These imaged results seem to corroborate the statistical results we obtained for Period 4.

5.3 Discussion

Before discussing results we must remember that this study deals only with one event, specifically the onset and early portion of the main phase of the event. Moreover, without nearby polar-orbiting satellite particle data, we cannot describe a definite cause-effect relationship. By using particle data from a geosynchronous satellite, we only get a general idea as to the near-earth particle environment, but what GOES-7 measures does not necessarily map down to earth at South Pole. Thus we are dealing with effects only, and for the effects observed, we will attempt to offer explanation for possible later verification.

Although not addressed earlier, we did perform the cross-correlation on the entire onset phase (1300-2000) and came up with a null result; *i.e.*, we found no evidence to contradict simultaneity of response across the 49-beam array. However, by breaking the onset phase into smaller pieces, we discovered a general pole-to-equator progression during a shorter period centered between 1430 and 1500. This effect seems to be coincident with a significant local maximum near 14:17, apparently in response to a short particle flux enhancement superimposed upon the already increasing particle flux. There are two possible mechanisms to consider when trying to explain the result: one involving a local change in field line geometry, and another involving the change in the particle energy (rigidity)

spectrum.

The first possible explanation may result from a local time effect coming into play such that field line configurations near local geomagnetic noon were altered. Recall that local geomagnetic noon for South Pole Station is at 1530 UT. Earlier, we discussed the midday recovery phenomenon, most dramatic near the auroral zone, and presumably caused by some local time variation in cutoff latitude (penetration depth). Perhaps the auroral oval or dayside cusp orientation relative to the station plays some role in changing from an open field line regime to a temporary closed field line regime over part or all of the array.

Meng's (1981) representation of the polar cusp location with respect to geomagnetic local time (Fig 5.13, shows the cusp centered just prior to noon and at approximately 74° invariant latitude. This happens to correspond roughly to the lag effect in Period 4. If the cusp happened to be located such that its equatorward edge was in the field of view, then presumably, the lower (equatorward) portion of the array would be in a closed field line regime, thus changing the local cutoff. In this scenario we would conclude that a temporary penetration depth gradient was established due to a local change in local field line associated with the dayside cusp.

The second possibility is that the particle rigidity spectrum somehow changed temporarily in association with the local enhancement centered at ~ 1447 . Previously, we discussed cutoff latitudes based on particle rigidity. We know that as geomagnetic latitude decreases the cutoff rigidity increases. Since our lags were concentrated near the bottom (lower latitude) of the array, we

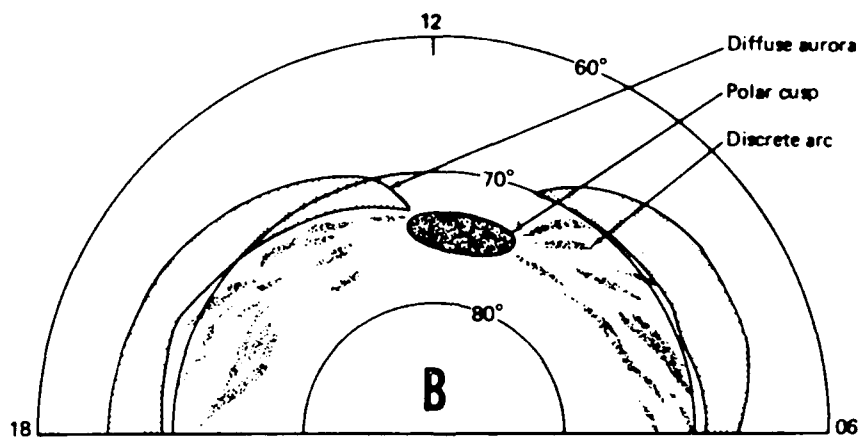


Figure 5.13: The polar dayside cusp relative to local geomagnetic time (from Meng, 1981).

might conclude that higher rigidity particles were either interrupted or experienced a lower flux. Assuming this to be the case, there would be a lower electron production rate at the lower latitude than before the change in rigidity spectrum occurred.

Unfortunately, we do not have digitized particle data at the time of this writing, so no adequate analysis of rigidity spectra is possible. Nor do we have particle precipitation data from low-orbiting polar satellites, which might help us define a cusp location. Therefore we cannot rule out either scenario. It is even possible that the delays may be due to a combination of the effects. Due to the limited data available as of this writing, this determination must be left for future investigations.

5.4 Suggestions for Future Research

Since this is only one event, there is plenty of room for further work to compare events. Some strategies to pursue for this particular event are as follows:

- Obtain low-altitude, polar-orbiting satellite particle data during the period in question to locate the cusp/auroral oval boundaries using particle precipitation measurements. We might be able to relate this information to our results, specifically the phenomenon near 1430–1500 UT.
- Obtain digitized particle data from GOES-7 or (preferably) from some platform located outside earth's magnetosphere and calculate energy or rigidity spectra for various times during the onset. Compare the spectra during the

1447 enhancement with earlier and later spectra and determine whether a significant difference exists.

- Perform a cross-correlation analysis between IRIS beams and several proton channels to determine whether correlation between particular beams and particular particle channels is a function of the beam's location in the array.

Additionally, as more IRIS data covering PCA events becomes available, it would be interesting to see if the delay associated with the enhancement near 1430–1500 was merely an isolated case, or if there are similar events. If other cases are discovered, we should wish to investigate both possible explanations offered in the previous section. Though the first possibility involving temporarily closed field lines is rather weak, we need to look at more events to rule out that possibility.

Finally, an IRIS system is now in operation at Sondrestromfjord, Greenland, near South Pole's conjugate point. This opens up new horizons for studying conjugate PCA effects using an imaging system.

As this was one of the first classic PCA events since the installation of IRIS in 1988, we are admittedly only scratching the surface with respect to its possible uses. By the end of this solar cycle, quite a bank of data should be available to compare and contrast PCAs and other absorption phenomena over South Pole Station and Sondrestromfjord.

References

- Akasofu, S.-I. and S. Chapman, *Solar Terrestrial Physics*, Oxford Clarendon Press, London, 1972.
- Armstrong, T.P., C.M. Laird, D. Venkatesan, S. Krishnaswamy, and T.J. Rosenberg, Interplanetary Energetic Ions and Polar Radio Wave Absorption, *J. Geophys. Res.*, **94**, 3543-3554, 1989.
- Bailey, D.K., Disturbances in the Lower Ionosphere Observed at VHF Following the Solar Flare of 23 Feb 1956 with Particular Reference to Auroral Zone Absorption, *J. Geophys. Res.*, **62**, 431-463, 1957.
- Bailey, D.K., Abnormal Ionization in the Lower Ionosphere Associated with Cosmic-Ray Flux Enhancements, *Proc. I.R.E.*, **47**, 255-271, 1959.
- Bailey, D.K., Polar Cap Absorption, *Planet. Space Sci.*, **12**, 495-541, 1964.
- Bruzek, A. and C.J. Durrant (eds.), *Illustrated Glossary for Solar and Solar-Terrestrial Physics*, D. Reidel Publishing Co., Boston, 1977.
- Chamberlain, J.W. and D.M. Hunten, *Theory of Planetary Atmospheres*, Academic Press, Inc., Orlando, Florida, 1987.
- Chapman, S., The Absorption and Dissociative of Ionizing Effect of Monochromatic Radiation in an Atmosphere on a Rotating Earth, *Proc. Phys. Soc*, **43**, 26-45, 1931.
- Chen, L. and A. Hasegawa, A Theory of Long-Period Pulsations 1. Steady

- State Excitation of Field Line Resonance, *J. Geophys. Res.*, **79**, 1024-1032, 1974.
- Davies, K., *Ionospheric Radio Propagation*, Dover Publications, Inc., New York, 1966.
- Dungey, J.W., Interplanetary Magnetic Field and the Auroral Zones, *Phys. Rev. Lett.*, **6**, 47-48, 1961.
- Detrick, D.L., Personal conversations, 1990.
- Detrick, D.L. and T.J. Rosenberg, A Phased-array Radiowave Imager for Studies of Cosmic Noise Absorption, *Radio Science*, to be published 1990.
- Duchon, C.E., Lanczos Filtering in One and Two Dimensions, *J. Appl. Meteorology*, **18**, 1016-1022, 1979.
- Evans, L.C. and E.C. Stone, Access of Solar Protons into the Polar Cap: A Persistent North-South Asymmetry, *J. Geophys. Res.*, **74**, 5127-5131, 1969.
- Freier, P.S., E.P. Ney, and J.R. Winckler, Balloon Observations of Solar Cosmic Rays on March 26, 1958, *J. Geophys. Res.*, **64**, 685-688, 1959.
- Gillmor, C.S., The Day-to-Night Ratio of Cosmic Noise Absorption during Polar Cap Absorption Events, *J. Atmos. Terr. Phys.*, **25**, 263-266, 1963.
- Gold, T., Plasma and Magnetic Fields in the Solar System, *J. Geophys. Res.*, **64**, 1665-1674, 1959.

- Goodman J. and D. Uffelman, HF Spectrum: New Concepts and Technologies, George Washington University, Washington, D.C., 1984.
- Hakura, Y., Entry of Solar Cosmic Rays into the Polar Cap Atmosphere, *J. Geophys. Res.*, **72**, 1461-1472, 1967.
- Hargreaves, J.K., The Upper Atmosphere and Solar-Terrestrial Relations, Van Nostrand Reinhold Co. Ltd., London, 1979.
- Heikkila, W.J., Definition of the Cusp, in The Polar Cusp, J.A. Holtet and A. Egeland (eds.), D. Reidel Publishing Company, Dordrecht, Holland, 1985.
- Hess, W.H. (ed.), Introduction to Space Science, Gordon and Breach Science Publishers, New York, 1965.
- Hultqvist, B., Auroral and Polar Cap Absorption, in Atmospheric Emissions, B.M. McCormac and A. Olmholz (eds.), Van Nostrand Reinhold, New York, 1969.
- Hundhausen, A.J., Coronal Expansion and Solar Wind, Springer-Verlag, Berlin, 1972.
- Krishnaswamy S., D.L. Detrick, and T.J. Rosenberg, The Inflection Point Method of Determining Riometer Quiet Day Curves, *Radio Science*, **20**, 123-136, 1985.
- Kundu, M.R. and F.T. Haddock, A Relation between Solar Radio Emission and Polar Cap Absorption of Cosmic Noise, *Nature*, **186**, 610-613, 1960.
- Leinbach, H., Midday Recoveries of Polar Cap Absorption, *J. Geophys.*

- Res.*, **72**, 5473-5483, 1967.
- Little, C.G. and H. Leinbach, The Riometer—a Device for Continuous Measurement of Ionospheric Absorption, *Proc. I.R.E.*, **47**, 315-320, 1959.
- McIlwain, C., Coordinates for Mapping the Distribution of Magnetically Trapped Particles, *J. Geophys. Res.*, **66**, 3681-3691, 1961.
- Meng, C-I., Electron Precipitation in the Midday Auroral Oval, *J. Geophys. Res.*, **86**, 2149-2174, 1981.
- Michel F.C. and A.J. Dessler, Physical Significance of Inhomogeneities in Polar Cap Absorption Events, *J. Geophys. Res.*, **70**, 4305-4311, 1965.
- Mitra, A.P., D-region in Disturbed Conditions Including Flares and Energetic Particles, *J. Atmos. Terr. Phys.*, **37**, 895-913, 1975.
- Mitra, A.P., Ionospheric Effects of Solar Flares, D. Reidel Publishing Co., Boston, 1974.
- Mitra, A.P. and C.A. Shain, The Measurement of Ionospheric Absorption Using Observations of 18.3 Mc/s Cosmic Radio Noise, *J. Atmos. Terr. Phys.*, **4**, 204-218, 1953.
- NSF, Survival in Antarctica, National Science Foundation, U.S. Government Printing Office, Washington, D.C., 1984.
- NASA, Meteorological Satellites—Past, Present, and Future, NASA Conference Publication 2227, 1982.

- NOAA, Solar-Geophysical Data Prompt Reports, Number 543, Part I,
November, 1989.
- Obayashi, T. and Y. Hakura, Propagation of Solar Cosmic Rays through
Interplanetary Magnetic Fields, *J. Geophys. Res.*, **65**, 3143-3148,
1960.
- Obayashi, T., Streaming of Solar Particles between Sun and Earth, *Planet.
Space Sci.*, **12**, 463-485, 1964.
- Panofsky, H.A., and G.W. Brier, Some Applications of Statistics to
Meteorology, Pennsylvania State University, 1958.
- Parker, E., Extension of the Solar Corona into Interplanetary Space, *J.
Geophys. Res.*, **64**, 1675-1681, 1958.
- Piddington, J.H., Cosmic Electrodynamics, Wiley and Sons, New York,
1969.
- Rairden, R.L., and S.B. Mende, Properties of 6300-Å Auroral Emissions
at South Pole, *J. Geophys. Res.*, **94**, 1402-1416, 1989.
- Ratcliffe, J.A., Sun, Earth, and Radio, McGraw-Hill Book Co., New York,
1970.
- Reid, G.C., A Diffusive Model for the Initial Phase of a Solar Proton
Event, *J. Geophys. Res.*, **69**, 2659-2667, 1964.
- Reid, G.C., in Physics of Geomagnetic Phenomena, Vol. 2, S. Matsushita
and W.H. Campbell (eds.), Academic Press, New York, 1967.
- Reid, G.C. and C. Collins, Observations of Abnormal VHF Radio Wave
Absorption at Medium and High Latitudes, *J. Atmos. Terr. Phys.*,

- 14, 63-81, 1959.
- Reid, G.C. and H. Leinbach, Morphology and Interpretation of the Great Polar Cap Absorption Events of May and July, 1959, *J. Atmos. Terr. Phys.*, **23**, 216-228, 1961.
- Reid, G.C. and H.H. Sauer, The Influence of the Geomagnetic Tail on Cosmic Ray Cutoffs, *J. Geophys. Res.*, **72**, 197-208, 1967a.
- Reid, G.C. and H.H. Sauer, Evidence for Nonuniformity of Solar Proton Precipitation over the Polar Caps, *J. Geophys. Res.*, **72**, 4383-4389, 1967b.
- Richmond, A.D., The Ionosphere, in The Solar Wind and the Earth, eds. S.-I. Akasofu and Y. Kamide, D. Reidel Publishing Company, Boston, 1987.
- Russell, C.T., The Magnetosphere, in The Solar Wind and the Earth, eds. S.-I. Akasofu and Y. Kamide, D. Reidel Publishing Company, Boston, 1987.
- SESC, SESC Glossary of Solar-Terrestrial Terms, USAF-NOAA Space Environment Services Center, Boulder, Colorado, 1988.
- Stix, M., The Sun—An Introduction, Springer-Verlag, Berlin, 1989.
- Stone, E.C., Local Time Dependence on Non-Störmer Cutoff for 1.5 MeV Protons in Quiet Geomagnetic Field, *J. Geophys. Res.*, **69**, 3577, 1964.
- Störmer, C., The Polar Aurora, Oxford Clarendon Press, London, 1955.
- Sturrock, P.A. (ed.), Solar Flares, Colorado Associated University Press,

- Boulder, Colorado, 1980.
- Svestka, Z., Solar Flares, D. Reidel Publishing Company, Boston, 1976.
- Townsend, R., R.W. Cannata, R.D. Prochaska, G.E. Rattray, J.C. Holbrook, Source Book of the Solar-Geophysical Environment, USAF Air Weather Service, AFGWC/TN-82/002, Offutt AFB, Nebraska, 1982.
- Van Allen, J.A. and L.A. Frank, Radiation Around the Earth to a Radial Distance of 107,400 km, *Nature*, **183**, 430-434, 1959.
- Van Allen, J.A., C.E. McIlwain, and G.H. Ludwig, Radiation Observations with Satellite 1958 ϵ , *J. Geophys. Res.*, **64**, 271-286, 1959.
- Van Allen, J.A., J.F. Fennell, and H.F. Ness, Asymmetric Access of Energetic Solar Protons to the Earth's North and South Polar Caps, *J. Geophys. Res.*, **76**, 4262-4275, 1971.
- Walker, J.J. and V.P. Bhatnagar, Ionospheric Absorption, Typical Ionization, Conductivity, and Possible Synoptic Heating Parameters in the Upper Atmosphere, *J. Geophys. Res.*, **94**, 3713-3720, 1989.
- Zmuda, A.J. and T.A. Potemra, Bombardment of the Polar-Cap Ionosphere by Solar Cosmic Rays, *Rev. Geophys. Space Phys.*, **10**, 981-991, 1972.